A&A, 702, A73 (2025)
https://doi.org/10.1051/0004-6361/202553984

Astronomy & Astrophysics

Euclid preparation

LXXIV. Euclidised observations of Hubble Frontier Fields and CLASH galaxy clusters

Euclid Collaboration: P. Bergamini[1,2,⋆], M. Meneghetti[2,3], G. Angora[4,5], L. Bazzanini[4,2], P. Rosati[4,2],
C. Grillo[1,6], M. Lombardi[1], D. Abriola[1], A. Mercurio[5,7,8], F. Calura[2], G. Despali[9,2,3], J. M. Diego[10],
R. Gavazzi[11,12], P. Hudelot[12], L. Leuzzi[9,2], G. Mahler[13,14,15], E. Merlin[16], C. Scarlata[17], N. Aghanim[18],
B. Altieri[19], A. Amara[20], S. Andreon[21], N. Auricchio[2], C. Baccigalupi[22,23,24,25], M. Baldi[26,2,3], S. Bardelli[2],
R. Bender[27,28], C. Bodendorf[27], D. Bonino[29], E. Branchini[30,31,21], M. Brescia[32,5,33], J. Brinchmann[34,35],
S. Camera[36,37,29], V. Capobianco[29], C. Carbone[6], J. Carretero[38,39], S. Casas[40], F. J. Castander[41,42],
M. Castellano[16], G. Castignani[2], S. Cavuoti[5,33], A. Cimatti[43], C. Colodro-Conde[44], G. Congedo[45],
C. J. Conselice[46], L. Conversi[47,19], Y. Copin[48], F. Courbin[49], H. M. Courtois[50], M. Cropper[51],
A. Da Silva[52,53], H. Degaudenzi[54], G. De Lucia[23], A. M. Di Giorgio[55], J. Dinis[52,53], M. Douspis[18],
F. Dubath[54], X. Dupac[19], S. Dusini[56], M. Farina[55], S. Farrens[57], S. Ferriol[48], M. Frailis[23], E. Franceschi[2],
M. Fumana[6], S. Galeotta[23], B. Garilli[6,⋆⋆], K. George[28], B. Gillis[45], C. Giocoli[2,58], A. Grazian[59],
F. Grupp[27,28], L. Guzzo[1,21], S. V. H. Haugan[60], W. Holmes[61], I. Hook[62], F. Hormuth[63], A. Hornstrup[64,65],
K. Jahnke[66], E. Keihänen[67], S. Kermiche[68], A. Kiessling[61], M. Kilbinger[57], B. Kubik[48], M. Kümmel[28],
M. Kunz[69], H. Kurki-Suonio[70,71], R. Laureijs[72], S. Ligori[29], P. B. Lilje[60], V. Lindholm[70,71], I. Lloro[73],
G. Mainetti[74], D. Maino[1,6,75], E. Maiorano[2], O. Mansutti[23], O. Marggraf[76], K. Markovic[61],
M. Martinelli[16,77], N. Martinet[11], F. Marulli[9,2,3], R. Massey[15], S. Maurogordato[78], E. Medinaceli[2], S. Mei[79],
Y. Mellier[80,12], G. Meylan[49], M. Moresco[9,2], L. Moscardini[9,2,3], E. Munari[23,22], R. Nakajima[76],
C. Neissner[81,39], S.-M. Niemi[72], J. W. Nightingale[82,15], C. Padilla[81], S. Paltani[54], F. Pasian[23], K. Pedersen[83],
V. Pettorino[72], S. Pires[57], G. Polenta[84], M. Poncet[85], L. A. Popa[86], L. Pozzetti[2], F. Raison[27], R. Rebolo[44,87],
A. Renzi[88,56], J. Rhodes[61], G. Riccio[5], E. Romelli[23], M. Roncarelli[2], E. Rossetti[26], R. Saglia[28,27],
Z. Sakr[89,90,91], A. G. Sánchez[27], D. Sapone[92], B. Sartoris[28,23], M. Schirmer[66], P. Schneider[76],
A. Secroun[68], E. Sefusatti[23,22,24], G. Seidel[66], S. Serrano[42,41,93], C. Sirignano[88,56], G. Sirri[3], L. Stanco[56],
J. Steinwagner[27], P. Tallada-Crespí[38,39], H. I. Teplitz[94], I. Tereno[52,95], R. Toledo-Moreo[96], F. Torradeflot[39,38],
I. Tutusaus[90], L. Valenziano[2,97], T. Vassallo[28,23], G. Verdoes Kleijn[98], A. Veropalumbo[21,31,99], Y. Wang[94],
J. Weller[28,27], G. Zamorani[2], E. Zucca[2], A. Biviano[23,22], M. Bolzonella[2], A. Boucaud[79], E. Bozzo[54],
C. Burigana[100,97], M. Calabrese[101,6], D. Di Ferdinando[3], J. A. Escartin Vigo[27], R. Farinelli[2], J. Gracia-Carpio[27],
N. Mauri[43,3], V. Scottez[80,102], M. Tenti[3], M. Viel[22,23,25,24,103], M. Wiesmann[60], Y. Akrami[104,105],
V. Allevato[5], S. Anselmi[56,88,106], M. Ballardini[4,2,107], M. Bethermin[108,11], A. Blanchard[90], L. Blot[109,106],
S. Borgani[110,22,23,24], A. S. Borlaff[111,112], S. Bruton[17], R. Cabanac[90], A. Calabro[16], G. Cañas-Herrera[72,113],
A. Cappi[2,78], C. S. Carvalho[95], T. Castro[23,24,22,103], K. C. Chambers[114], S. Contarini[27], T. Contini[90],
A. R. Cooray[115], O. Cucciati[2], B. De Caro[6], G. Desprez[116], A. Díaz-Sánchez[117], S. Di Domizio[30,31],
H. Dole[18], S. Escoffier[68], A. G. Ferrari[43,3], I. Ferrero[60], F. Finelli[2,97], F. Fornari[97], L. Gabarra[118],
K. Ganga[79], J. García-Bellido[104], V. Gautard[119], E. Gaztanaga[41,42,120], F. Giacomini[3], G. Gozaliasl[121,70],
A. Hall[45], H. Hildebrandt[122], J. Hjorth[123], M. Huertas-Company[44,124,125,126], A. Jimenez Muñoz[127],
J. J. E. Kajava[128,129], V. Kansal[130,131], D. Karagiannis[132,133], C. C. Kirkpatrick[67], L. Legrand[134], G. Libet[85],
A. Loureiro[135,136], G. Maggio[23], M. Magliocchetti[55], C. Mancini[6], F. Mannucci[137], R. Maoli[138,16],
C. J. A. P. Martins[139,34], S. Matthew[45], L. Maurin[18], R. B. Metcalf[9,2], P. Monaco[110,23,24,22],
C. Moretti[25,103,23,22,24], G. Morgante[2], Nicholas A. Walton[140], J. Odier[127], L. Patrizii[3], A. Pezzotta[27],
M. Pöntinen[70], V. Popa[86], C. Porciani[76], D. Potter[141], I. Risso[99], P.-F. Rocci[18], M. Sahlén[142],
A. Schneider[141], M. Sereno[2,3], P. Simon[76], A. Spurio Mancini[143,51], S. A. Stanford[144], C. Tao[68], G. Testera[31],

---

[⋆] Corresponding author: `pietro.bergamini@inaf.it`

[⋆⋆] Deceased.

R. Teyssier[145], S. Toft[65,146,147], S. Tosi[30,31], A. Troja[88,56], M. Tucci[54], C. Valieri[3], J. Valiviita[70,71], D. Vergani[2], and G. Verza[148,149]

(Affiliations can be found after the references)

Received 31 January 2025 / Accepted 16 June 2025

ABSTRACT

We present `HST2EUCLID`, a novel `Python` code to generate *Euclid* realistic mock images in the $H_{\rm E}$, $J_{\rm E}$, $Y_{\rm E}$, and $I_{\rm E}$ photometric bands based on panchromatic *Hubble* Space Telescope observations. The software was used to create a simulated database of *Euclid* images for the 27 galaxy clusters observed during the Cluster Lensing And Supernova survey with *Hubble* (CLASH) and the Hubble Frontier Fields (HFF) program. Since the mock images were generated from real observations, they incorporate, by construction, all the complexity of the observed galaxy clusters. The simulated *Euclid* data of the galaxy cluster MACS J0416.1−2403 were then used to explore the possibility of developing strong lensing models based on the *Euclid* data. In this context, complementary photometric or spectroscopic follow-up campaigns are required to measure the redshifts of multiple images and cluster member galaxies. By Euclidising six parallel blank fields obtained during the HFF program, we provide an estimate of the number of galaxies detectable in *Euclid* images per deg^2 per magnitude bin (number counts) and the distribution of the galaxy sizes. Finally, we present a preview of the *Chandra* Deep Field South that will be observed during the Euclid Deep Survey and two examples of galaxy-scale strong lensing systems residing in regions of the sky covered by the Euclid Wide Survey. The methodology developed in this work lends itself to several additional applications, as simulated *Euclid* fields based on HST (or JWST) imaging with extensive spectroscopic information can be used to validate the feasibility of legacy science cases or to train deep learning techniques in advance, thus preparing for a timely exploitation of the Euclid Survey data.

Key words. gravitational lensing: strong – galaxies: clusters: general – cosmology: observations – dark matter

1. Introduction

Galaxy clusters, the most powerful gravitational lenses in the Universe, can distort dozens of background sources simultaneously, producing gravitational arcs and multiple images (e.g. Bergamini et al. 2021). Researchers routinely use these features to constrain the total mass distribution in cluster cores.

Various algorithms, including parametric and free form methods, have been developed for this task (e.g. Kneib et al. 1993; Bradač et al. 2005; Diego et al. 2005; Liesenborgs et al. 2006; Coe et al. 2008; Jullo et al. 2007; Zitrin & Broadhurst 2009; Oguri 2010; Zitrin et al. 2013; Lam et al. 2014). Parametric models represent the cluster's total mass distribution as a collection of mass components, each characterised by parameters varied to fit the strong lensing constraints. These components account for cluster-scale dark matter haloes and the galaxy-scale substructure traced by cluster member galaxies. In contrast, the free-form approach often employs meshes or radial-basis functions to depict the cluster's total mass distributions. Several of these techniques are discussed and compared in Meneghetti et al. (2017). Bergamini et al. (2019) suggested combining strong lensing with stellar velocity dispersion measurements of cluster galaxies, obtained from the Multi Unit Spectroscopic Explorer (MUSE, at the Very Large Telescope, Bacon et al. 2012) spectra, to enhance the precision of mass models on smaller scales (see also Bergamini et al. 2021; Meneghetti et al. 2020, 2022, 2023; Granata et al. 2022). These additional data help reduce degeneracies between large- and small-scale cluster mass components. Accurate reconstruction of the inner cluster mass distribution is essential for enabling a variety of astrophysical and cosmological applications of strong lensing by galaxy clusters, including studying the nature of dark matter, examining the interplay between baryons and dark matter, exploring cosmic structure formation and evolution, constraining cosmological parameters, and utilising galaxy clusters as cosmic telescopes (see Kneib & Natarajan 2011; Meneghetti et al. 2013; Bartelmann et al. 2013; Moresco et al. 2022, for extensive reviews).

Until recently, only a few tens of galaxy clusters could be accurately modelled for their total mass distributions. Strong lensing modelling requires high spatial resolution and deep observations, previously achievable mainly by the *Hubble* Space Telescope (HST) and, more recently, the *James Webb* Space Telescope (JWST). Most known strong lensing clusters were identified in ground-based observations (e.g. Bayliss et al. 2011), or by following up on galaxy clusters pre-selected based on their X-ray emission or the Sunyaev–Zeldovich effect amplitude (Ebeling et al. 2001, 2007, 2010; Planck Collaboration XXVII 2016). Confirming strong lensing features and measuring their redshifts required additional data from the HST (or JWST) and spectrographs on large telescopes.

This situation is set to change dramatically. Since last year, *Euclid* has been observing most of the extragalactic sky with spatial resolution in the $I_{\rm E}$ band comparable to that of HST (Laureijs et al. 2011; Euclid Collaboration: Scaramella et al. 2022). The Euclid Wide Survey (EWS) aims to cover about 15 000 deg^2 of the extragalactic sky to a minimum depth of $m_{\rm AB} = 24.5$ mag in the $I_{\rm E}$ band (Cropper et al. 2016), with a signal-to-noise ratio (S/N) of 10 for extended sources. *Euclid* will also survey the same area in the near-infrared $Y_{\rm E}$, $J_{\rm E}$, and $H_{\rm E}$ bands (Maciaszek et al. 2022) to a depth of $m_{\rm AB} = 24.0$ mag with a minimum S/N of 5 for point sources. Additionally, its slitless spectroscopy will detect line emission with a sensitivity of $f_{{\rm H}\alpha} \gtrsim 2 \times 10^{-16}\,{\rm erg\,s^{-1}cm^{-2}}$ and a S/N of 3.5 for a typical source of size $0\farcs5$.

The primary goal of *Euclid* is to reveal the nature of dark energy and dark matter, the two dominant components of the Universe, using weak lensing and galaxy clustering as the main probes. However, *Euclid* will also significantly contribute to the discovery of galaxy clusters. During its lifetime, *Euclid* is expected to observe over 60 000 galaxy clusters (Sartoris et al. 2016), with a S/N greater than 3, in the redshift range $0.2 \le z \le 2$. About 5000 of these clusters are anticipated to be strong gravitational lenses containing multiple families of lensed images of background sources and strongly distorted radial and tangential arcs (Boldrin et al. 2012, 2016). Developing accurate strong

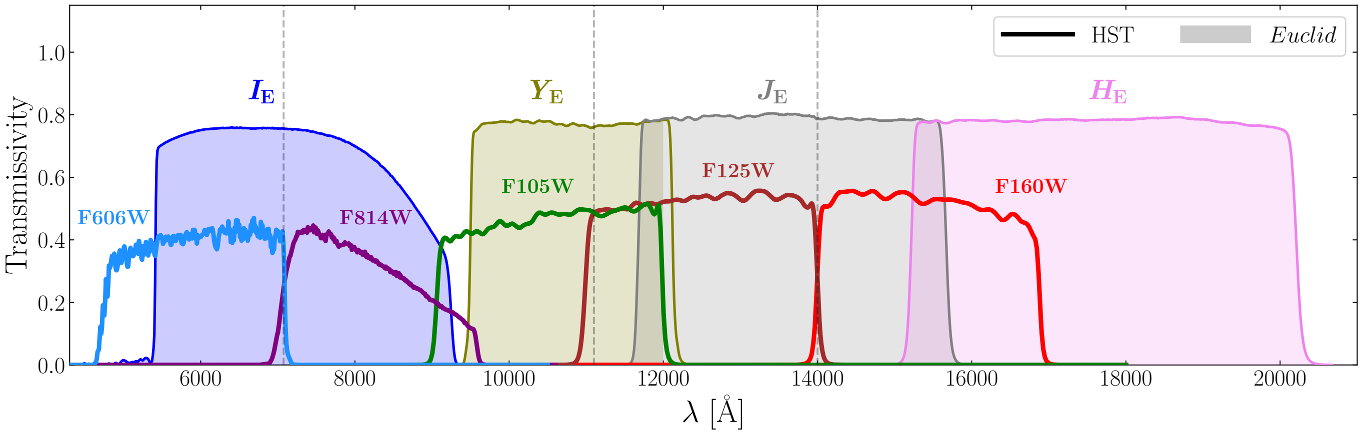

Fig. 1. Transmission curves of HST and *Euclid* filters considered in this work. The five HST filters F606W, F814W, F105W, F125W, and F160W are shown with coloured solid lines, while the four *Euclid* bands $I_{\rm E}$, $Y_{\rm E}$, $J_{\rm E}$, and $H_{\rm E}$ are represented by the coloured areas. The vertical black dashed lines indicate the wavelengths where the response of the HST F814W, F125W, and F160W filters begins to dominate over the F606W, F105W, and F125W filters, respectively.

lensing models for even a subset of this large number of cluster lenses will provide critical insights into the nature of dark matter and the growth of cosmic structures, provided that a large number of multiple images and cluster member galaxies can be identified from *Euclid* observations.

This work introduces a tool to convert HST observations into *Euclid*-like imaging data. We focus on HST observations of massive galaxy clusters collected in the Cluster Lensing and Supernova Survey with Hubble (CLASH[1], Postman et al. 2012) and the Hubble Frontier Fields (HFF[2], Lotz et al. 2014, 2017) programmes. We produced a simulated dataset from these images, consisting of mock observations of the same clusters in the EWS. We used simulated observations for the galaxy cluster MACS J0416.1−2403 (hereafter, MACS J0416) to quantify the number of strong lensing features detectable in future *Euclid* observations of lens galaxy clusters. These are then used to preliminarily test the strengths and weaknesses of *Euclid*-based cluster strong lensing models. Finally, the HFF parallel fields are employed to estimate the magnitude and size distributions of the luminous sources detectable in the *Euclid* images.

The paper is organised as follows. In Sect. 2, we present the HST observational dataset used as input for the simulations. The simulation pipeline is detailed in Sect. 3. In Sect. 4, we describe various tests conducted on the mock *Euclid* images to validate the simulations. In Sect. 5, we present *Euclid*-based strong lensing models for the galaxy cluster MACS J0416, and the results of the strong lensing analysis are reported in Sect. 6. In Sect. 7, we discuss other applications of the *Euclid* simulated images, and the main conclusions of this work are outlined in Sect. 8. Throughout this work, magnitudes are given in the AB system (Oke & Gunn 1983).

2. Input data

The simulated *Euclid* database of galaxy cluster observations presented in this work is based on the photometric data collected by the HST during the CLASH and HFF programmes. The former is a multi-cycle treasury programme that provided panchromatic images of 25 massive galaxy clusters in the redshift range [0.187, 0.890], for a total of 524 orbits from November 2010 to July 2013. The observations were carried out in 16 photometric bands ranging from UV to NIR wavelengths, using the Advanced Camera for Surveys (ACS, with filters: F435W, F475W, F606W, F625W, F775W, F814W, and F850W) and the Wide-Field Camera-3 (WFC3, with filters: F105W, F110W, F125W, F140W, F160W, F225W, F275W, F336W, and F390W). The HFF programme provided deeper HST observations (840 HST orbits) of six massive clusters (four in common with CLASH), selected among the strongest known gravitational lenses, in seven ACS (F435W, F606W, and F814W) and WFC3 (F105W, F125W, F140W, and F160W) bands. The depth of the HFF images corresponds to a limiting magnitude of $m_{\rm AB}\sim 29$ with a S/N of 5 for point sources within an aperture of $0\farcs2$ radius. This depth is about 1.5 magnitudes deeper than the CLASH observations.

We note that the HFF and CLASH imaging is much deeper than the *Euclid* observations we wish to produce, as discussed in the following sections. The images used in this work are drizzled to pixel scales of 65 mas px^{-1} and 60 mas px^{-1} for the CLASH and HFF data, respectively.

3. Simulation pipeline

This section describes the `Python`[3] code `HST2EUCLID` developed to simulate realistic *Euclid* images from HST multi-band observations. Although our primary use in this work is the production of mock *Euclid* observations of galaxy clusters, `HST2EUCLID` is generally applicable to convert every sufficiently deep HST image into a *Euclid*-like observation, with the only requirement being that the available HST bands overlap with the *Euclid* photometric filters to be simulated (see Fig. 1). In particular, the HST F606W and F814W filters were used to simulate the *Euclid* $I_{\rm E}$ band, while from the HST F105W, F125W, and F160W filters we simulate the $Y_{\rm E}$, $J_{\rm E}$, and $H_{\rm E}$ bands (see Sect. 3.3). In Sect. 6, we present selected examples of *Euclid* observations different from galaxy cluster fields.

Figure 2 visually summarises the different steps of the simulation pipeline (labelled a to e) implemented in the `HST2EUCLID` code. These are described in detail in the following subsections, adopting the same letters as in Fig. 2, for clarity.

---

[1] https://archive.stsci.edu/prepds/clash/

[2] https://archive.stsci.edu/prepds/frontier/

[3] https://www.python.org/

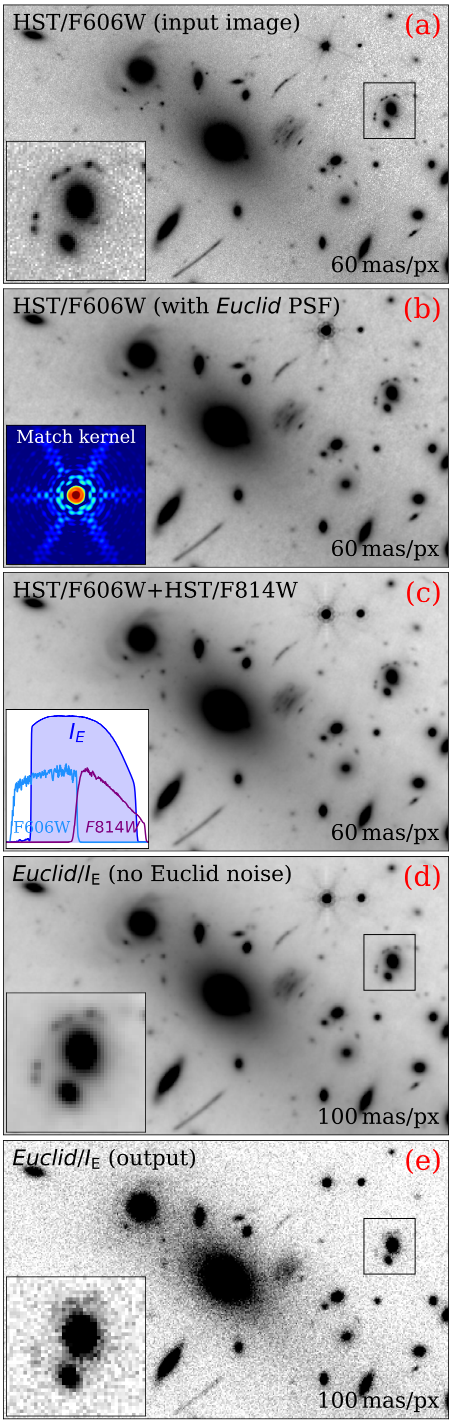

Fig. 2. Steps of the Euclidisation pipeline. In the top panel (a), we show the original *Hubble* F606W image of the galaxy cluster MACS J0416 at $z = 0.396$. The bottom panel (e) shows the final simulated I_E band. The intermediate panels (b), (c), and (d), from top to bottom, illustrate: the convolution to match the *Euclid* PSF, the result of combining the *Hubble* F606W and F814W filters to produce the I_E band, and the rebinning necessary to match the *Euclid* pixel scale in the I_E band (see Sect. 3).

3.1. STEP a: Conversion of HST images to flux densities and image alignment

In this first step of the Euclidisation pipeline, we converted the pixel values of the HST images from units of electrons per second ($\mathrm{e\,s^{-1}}$) to physical flux densities ($\mathrm{erg\,s^{-1}\,cm^{-2}\,Hz^{-1}}$). The conversion was performed using the following equation:

$$f[\mathrm{erg\,s^{-1}\,cm^{-2}\,Hz^{-1}}] = F[\mathrm{e\,s^{-1}}] \times 10^{-0.4\,(\mathrm{ZP_{HST}}+48.6)}, \tag{1}$$

where $\mathrm{ZP_{HST}}$ is the instrumental HST zero point, defined as the AB magnitude of an object producing a signal of one electron per second in the HST image. The $\mathrm{ZP_{HST}}$ value was computed from the pivot wavelength (`PHOTPLAM`) and the inverse sensitivity (`PHOTFLAM`), whose values are provided in the header of the HST Flexible Image Transport System (FITS, Pence et al. 2010) files. Specifically, we used[4]:

$$\begin{aligned}\mathrm{ZP_{HST}} = &-2.5\log_{10}(\texttt{PHOTFLAM})\\ &-5\log_{10}(\texttt{PHOTPLAM}) - 2.4079.\end{aligned} \tag{2}$$

Subsequently, we co-aligned the HST images in the different bands so that they shared the same pixel grid and astrometric calibration. For this purpose, we used the `Python` function `reproject_exact` of the module `reproject`[5].

3.2. STEP b: Matching the HST and Euclid point spread functions

The HST point spread functions (PSFs) have different shapes and full width at half maximum (FWHM) compared with the corresponding *Euclid* PSFs[6]. These differences must be taken into account to simulate realistic *Euclid* observations. For each HST band, we derived a kernel function (hereafter, matching kernel) which, when convolved with the corresponding HST images, reproduced the correct PSF in the *Euclid* simulated data.

The matching kernels between corresponding pairs of HST and *Euclid* PSFs (see Sect. 3.3) were computed using the `Python` function `create_matching_kernel` of the `Photutils` package (Bradley et al. 2023)[7]. The HST PSF models were obtained with the `TinyTim` software[8]. Although we verified that these PSFs yielded accurate results, `HST2EUCLID` allows users full flexibility to implement alternative or customised PSF models. In panel (b) of Fig. 2, we show the effect of convolving the HST/F606W image of the galaxy cluster MACS J0416 with the corresponding matching kernel (shown in the inset of the same panel) to the I_E band.

3.3. STEP c: Combination of HST filters to generate the Euclid bands

In this step, we expressed the flux in a *Euclid* band Q as a linear combination of N fluxes in nearby HST filters $\{\mathrm{R}_j\}$:

$$F_\mathrm{Q} = \sum_{j=1}^{N} w_j\, F_{\mathrm{R}_j} = \boldsymbol{w}^\mathrm{T} \boldsymbol{F}_\mathbf{R}, \tag{3}$$

---

[4] www.stsci.edu/hst/instrumentation/acs/data-analysis/zeropoints

[5] https://reproject.readthedocs.io/en/stable/

[6] The FWHM values of the HST PSFs in the F606W, F814W, F105W, F125W, and F160W filters range from approximately 70 mas to 130 mas. These values are smaller than those of the Euclid bands at comparable wavelengths (for example, Euclid Collaboration: Mellier et al. 2025 report a measured PSF FWHM of 130 mas in the I_E band). Therefore, we can reliably match the HST resolution to that of Euclid by convolving the HST images with the appropriate matching kernels.

[7] https://photutils.readthedocs.io/en/stable/api/photutils.psf.matching.create_matching_kernel.html

[8] https://www.stsci.edu/hst/instrumentation/focus-and-pointing/focus/tiny-tim-hst-psf-modeling

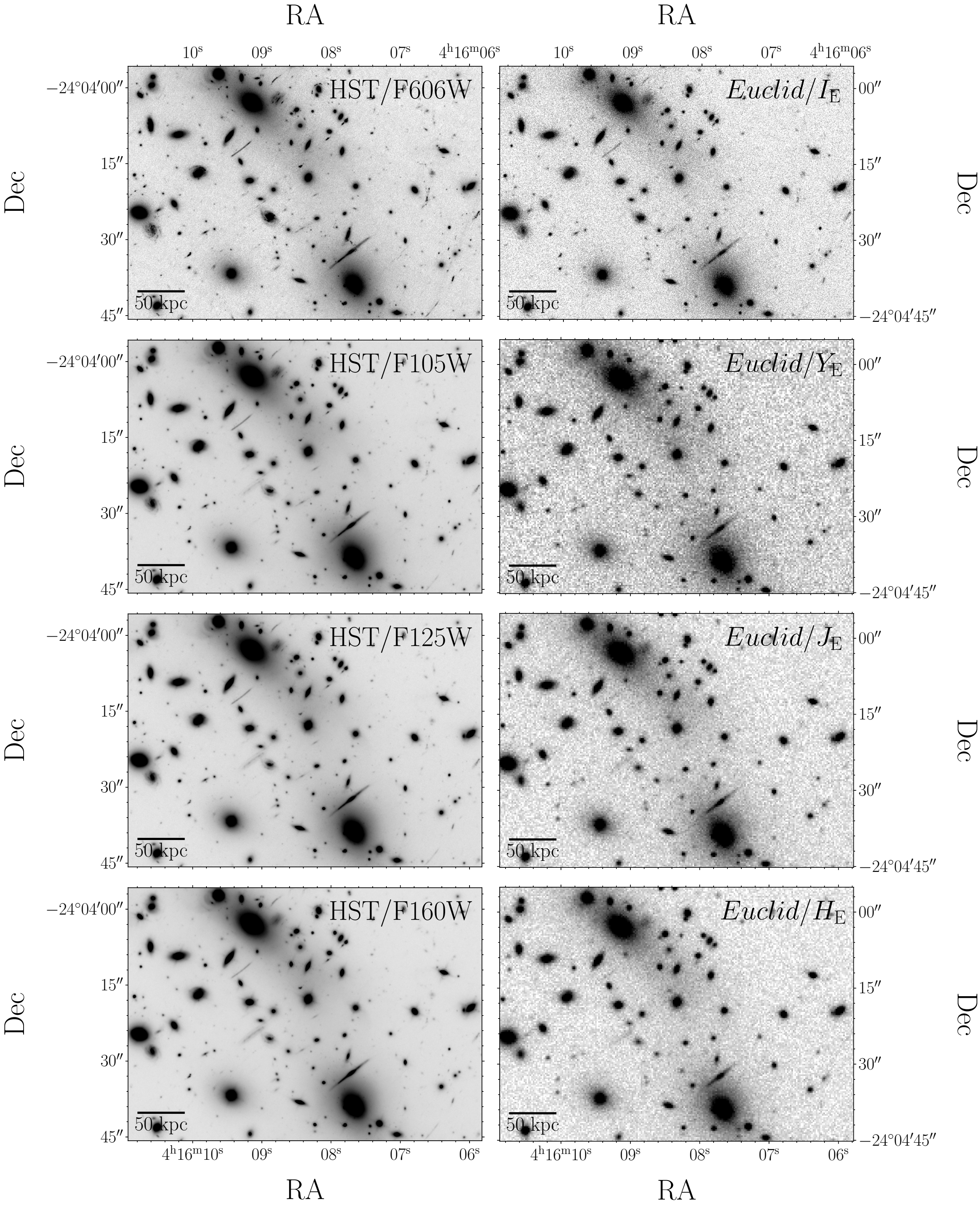

Fig. 3. Images of the galaxy cluster MACS J0416 in different photometric filters, observed with HST (left column) and *Euclid* (right column). The *Euclid* images are simulated using the pipeline described in Sect. 3, starting from the HST observations in the left column panels including the F814W filter, which is not displayed.

where the final term is expressed in linear algebra notation, with $\boldsymbol{w}$ and $\boldsymbol{F}_\mathbf{R}$ denoting column vectors. Below, we derive an expression for the weight vector $\boldsymbol{w}$.

We assumed that the spectral density of flux $f(\lambda)$, – defined as the energy per unit time, per unit spherical angle, per unit detector area, per unit wavelength emitted by a source, (or $f(\nu)$ if it is expressed in terms of unit frequency) – could be described as a linear combination of N base functions $\{f_i(\lambda)\}$ (or $\{f_i(\nu)\}$):

$$f(\lambda) = \sum_{i=1}^{N} k_i f_i(\lambda) = \frac{c}{\lambda^2} \sum_{i=1}^{N} k_i f_i(\nu). \tag{4}$$

Here, k_i are constants associated with the decomposition of the spectral flux density. In computing the last term, we note that $f_i(\lambda)$ can be expressed as a function of frequency as

$$f_i(\lambda) = (c/\lambda^2) f_i(\nu), \tag{5}$$

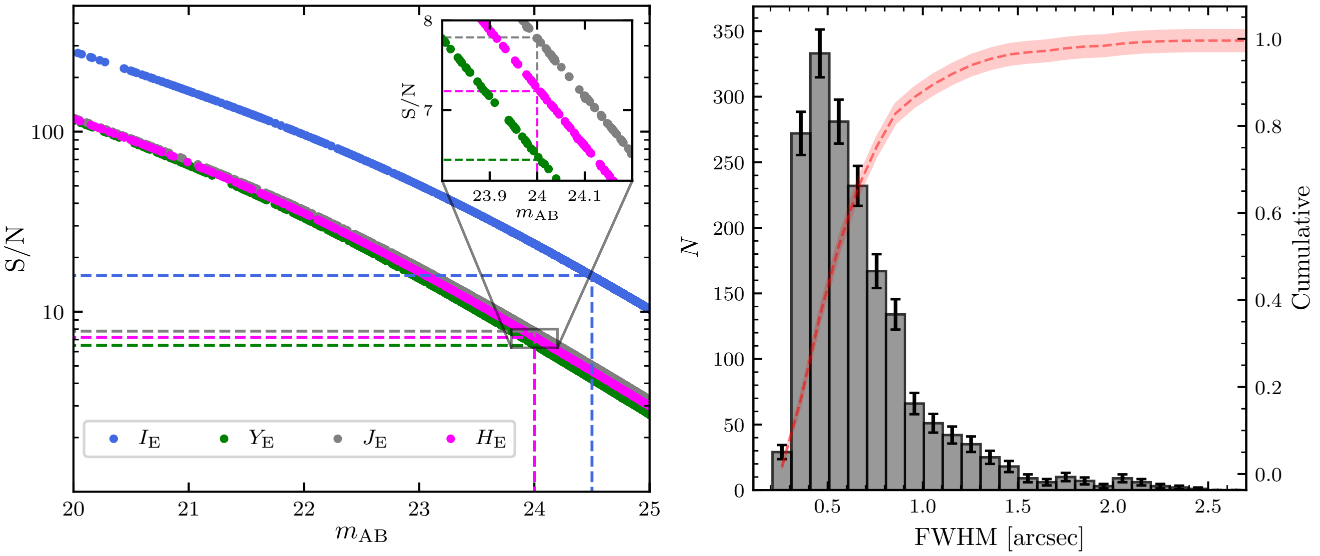

Fig. 4. Left: Signal-to-noise ratio (S/N) as a function of the magnitude for the luminous sources detected in the *Euclid* simulated images of the galaxy cluster MACS J0416. Blue, green, grey, and magenta dots indicate the S/N for galaxies detected in the *Euclid* I_{E}, Y_{E}, J_{E}, and H_{E} images, respectively, as a function of their magnitude in the different bands. These quantities are measured within circular apertures of radius $0\farcs65$ for the I_{E} band, and radius $0\farcs51$ (equivalent in extension to the $0\farcs9 \times 0\farcs9$ aperture quoted in Table 1) for the Y_{E}, J_{E}, and H_{E} filters. Vertical and horizontal dashed lines mark the values of the limiting S/Ns ($(\mathrm{S/N})_{\mathrm{lim}}^{I_{\mathrm{E}}} = 15.9$, $(\mathrm{S/N})_{\mathrm{lim}}^{Y_{\mathrm{E}}} = 6.5$, $(\mathrm{S/N})_{\mathrm{lim}}^{J_{\mathrm{E}}} = 7.8$, and $(\mathrm{S/N})_{\mathrm{lim}}^{H_{\mathrm{E}}}$=7.2) and limiting magnitudes ($m_{\mathrm{lim}}^{I_{\mathrm{E}}} = 24.5$, $m_{\mathrm{lim}}^{Y_{\mathrm{E}}} = 24.0$, $m_{\mathrm{lim}}^{J_{\mathrm{E}}} = 24.0$, and $m_{\mathrm{lim}}^{H_{\mathrm{E}}} = 24.0$). Right: Full width at half maximum (FWHM) distribution (grey) and its cumulative probability distribution (red) estimated for 1748 galaxies in six HFF parallel fields with I_{E} magnitude ≤ 24.5 (i.e. brighter than the limiting magnitude in the I_{E} filter).

with c being the light velocity in vacuum. We can then express both F_{Q} and F_{R_j} as

$$\begin{aligned} F_{\mathrm{R}_j} &= \sum_i \mathcal{R}_{ij} k_i\,, \quad \text{or} \quad \boldsymbol{F}_{\mathbf{R}} = \mathcal{R}\boldsymbol{k}\,, \\ F_{\mathrm{Q}} &= \sum_i q_i k_i = \boldsymbol{q}^{\mathrm{T}}\,\boldsymbol{k}, \end{aligned} \tag{6}$$

where the matrix $\mathcal{R}$ is associated with the transmissivity of the HST filters, as detailed below. Assuming the AB magnitude system, all quantities above can be computed as (see Eq. (4) of Hogg et al. 2002)

$$\mathcal{R}_{ij} = \frac{1}{c\, g_\nu^{\mathrm{AB}}} \frac{\int \mathrm{d}\lambda\, \lambda\, f_i(\lambda)\, R_j(\lambda)}{\int \frac{\mathrm{d}\lambda}{\lambda}\, R_j(\lambda)}, \tag{7}$$

$$q_i = \frac{1}{c\, g_\nu^{\mathrm{AB}}} \frac{\int \mathrm{d}\lambda\, \lambda\, f_i(\lambda)\, Q(\lambda)}{\int \frac{\mathrm{d}\lambda}{\lambda}\, Q(\lambda)}, \tag{8}$$

where g_ν^{AB} is the zero point for the AB magnitude system (g_ν^{AB} = 3631 Jy, where 1 Jy = $10^{-26}\,\mathrm{W\,m^{-2}\,Hz^{-1}}$), and $R_j(\lambda)$ and $Q(\lambda)$ are the transmissivities of the HST and *Euclid* photometric bandpasses, respectively (see Fig. 1).

By combining the two expressions in Eq. (6), we obtained[9]

$$F_{\mathrm{Q}} = \boldsymbol{q}^{\mathrm{T}}\,\boldsymbol{k} = \boldsymbol{q}^{\mathrm{T}}\,\mathcal{R}^{-1}\,\boldsymbol{F}_{\mathbf{R}}. \tag{9}$$

Finally, by inserting this equation into Eq. (3), we derived the following general expression for the weights:

$$\boldsymbol{w} = (\boldsymbol{q}^{\mathrm{T}}\,\mathcal{R}^{-1})^{\mathrm{T}} = \mathcal{R}^{-\mathrm{T}}\boldsymbol{q}. \tag{10}$$

In Fig. 1, we present the transmission functions of the *Euclid* photometric bands (I_{E}, Y_{E}, J_{E}, and H_{E}, Euclid Collaboration: Schirmer et al. 2022) along with the HST filters used for simulations that cover a similar wavelength range to *Euclid* (F606W, F814W, F105W, F125W, and F160W). The figure highlights that the wavelength range of the Y_{E} band is well aligned with the HST F105W filter, while the H_{E} band overlaps solely with the F160W filter. For both cases, we assumed that the spectral density of flux per unit frequency, $f(\nu)$, of the sources in the images remains constant over the entire wavelength range covered by the input (R_1) and output (Q_1) filters, i.e. $f(\lambda) \propto c/\lambda^2$. For the H_{E} band, this assumption, necessitated by the absence of HST data covering the reddest part of the H_{E} band (see Fig. 1), is crucial to correctly recovering the measured magnitudes of the luminous sources in the simulated field. However, this represents a rough approximation of the true flux in the real H_{E} band, as it lacks photometric information from the source spectra at $\lambda > 17\,000$ Å. Notably, Balmer break galaxies at redshift $z > 3$ would appear brighter in H_{E} than in the F160W band. Under the previous assumption, $\mathcal{R}$ and $\boldsymbol{q}$ are one-dimensional matrices with $\mathcal{R} = \boldsymbol{q}$ = const. and $\boldsymbol{w}$ = 1. Thus, the magnitudes of the sources in the Y_{E} and H_{E} *Euclid* bands are identical to those in the F105W and F160W HST filters, respectively.

In contrast, the I_{E} and J_{E} transmission functions span two HST bands. Specifically, the I_{E} band overlaps with both the F606W and F814W filters, while the J_{E} band overlaps with the F125W and F160W filters. In these cases, the weights, $\boldsymbol{w}$, were computed by assuming that the spectral density of flux, $f(\lambda)$, could be modelled as a sum of two top-hat functions $f_{\{1,2\}}(\nu)$ (see Eq. (4)). The $f_1(\nu)$ base function is assumed to be constant within one of the two input HST bands and zero outside, while the opposite holds for $f_2(\nu)$. In this scenario, $\mathcal{R}$ is a two-dimensional matrix with $\mathcal{R} \propto \mathbb{I}$, where $\mathbb{I}$ represents the identity matrix, and the weights, w_j, assume the following values:

---

[9] A necessary condition for the matrix $\mathcal{R}$ to be invertible is that the number of input filters has to be equal to the number of $f_i(\lambda)$ functions in Eq. (4) (i.e. $\mathcal{R}$ has to be a square matrix).

Table 1. Relevant quantities of the EWS.

Euclid wide survey (EWS)					
Euclid band	$t_{\rm exp}$ [s]	$m_{\rm lim}$	$\mathrm{SN}_{\rm lim}$	Aperture size	$N_{\rm ap}^{\rm px}$
$I_{\rm E}$	2280	24.5	15.9	$r = 0\farcs65$	132.7
$Y_{\rm E}$	448	24	6.5	$0\farcs9 \times 0\farcs9$	9
$J_{\rm E}$	448	24	7.8	$0\farcs9 \times 0\farcs9$	9
$H_{\rm E}$	448	24	7.2	$0\farcs9 \times 0\farcs9$	9

Notes. The values are reported by Euclid Collaboration: Scaramella et al. (2022). The total exposure time for each *Euclid* band is denoted by $t_{\rm exp}$, and $\mathrm{SN}_{\rm lim}$ indicates the S/N of a source with a magnitude $m_{\rm lim}$, measured within an aperture with a total area (in pixels) equal to $N_{\rm ap}^{\rm px}$. A circular aperture of radius $0\farcs65$ is used for $I_{\rm E}$ images, while square apertures of $0\farcs9 \times 0\farcs9$ are used for $Y_{\rm E}$, $J_{\rm E}$, and $H_{\rm E}$ images.

$$
\begin{aligned}
w_{\mathrm{F606W}\rightarrow I_{\rm E}} &= 0.542, \\
w_{\mathrm{F814W}\rightarrow I_{\rm E}} &= 0.458, \\
w_{\mathrm{F125W}\rightarrow J_{\rm E}} &= 0.617, \\
w_{\mathrm{F160W}\rightarrow J_{\rm E}} &= 0.383.
\end{aligned}
\tag{11}
$$

We note that, according to the previous hypotheses, the weights corresponding to the same *Euclid* band sum to one. In panel (c) of Fig. 2, we show the result of combining the two HST F606W and F814W filters into a single image, obtained using Eq. (3).

3.4. STEP d: Projection onto the Euclid pixel grid

In this step, we re-binned the images from the HST pixel grid to the correct *Euclid* pixel scale. To this aim, we employed the `Python` function `reproject_exact` introduced above. The resulting images have pixel scales of 100 mas px^{-1} in the $I_{\rm E}$ band and 300 mas px^{-1} in $Y_{\rm E}$, $J_{\rm E}$, and $H_{\rm E}$ filters.

The re-binned images, expressed in units of physical flux, were then converted into units of electrons per second by inverting Eq. (1). For this conversion, we assumed a zero point of $\mathrm{ZP}_{\rm Euclid} = 23.9$ mag for all bands. The resulting surface brightness per pixel in the *Euclid* band X is hereafter denoted as $F_{X,\rm rebin}$. Panel (d) of Fig. 2 illustrates the result of the re-binning procedure for the $I_{\rm E}$ band.

3.5. STEP e: Noise addition

The final step of the Euclidisation pipeline involved incorporating the appropriate noise into the *Euclid* simulated images. To accomplish this, we assumed that the noise in the input HST background subtracted images was negligible compared to the final noise. This approximation is supported by the significantly greater depth of the HST observations compared to that of the *Euclid* images.

The noise level was determined by adjusting the sky surface brightness of the *Euclid* images to achieve the expected nominal S/N for a source with a specific limiting magnitude. Specifically, to measure a S/N of $\mathrm{SN}_{\rm lim}$ for a source with flux of $F_{\rm lim}\,[\mathrm{e\,s^{-1}}]$ measured within an aperture containing $N_{\rm ap}^{\rm px}$ pixels, the sky surface brightness per pixel in units of $[\mathrm{e\,s^{-1}}]$ was calculated as

$$
\begin{aligned}
\mathrm{BK_{sky}}[\mathrm{e\,s^{-1}}] = &\left\{\left(F_{\rm lim}[\mathrm{e\,s^{-1}}]\right)^2 \times t_{\rm exp} \times (\mathrm{SN}_{\rm lim})^{-2} - F_{\rm lim}[\mathrm{e\,s^{-1}}]\right\} \\
&\times \left(N_{\rm ap}^{\rm px}\right)^{-1},
\end{aligned}
\tag{12}
$$

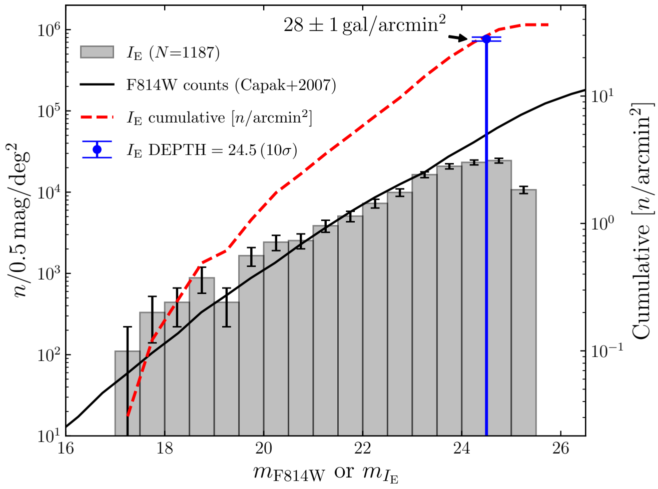

Fig. 5. Galaxy number counts from *Euclid* observations. The galaxy differential number counts derived from the simulated *Euclid* observations in the $I_{\rm E}$ band of the six HFF parallel fields are shown by the grey histogram with error bars. For comparison, those measured from HST observations (Capak et al. 2007) are indicated by the black solid line. The vertical blue line marks the limiting magnitude in the $I_{\rm E}$ band (24.5 at $10\,\sigma$). The cumulative number of galaxies per $\mathrm{arcmin^2}$ is shown by the red dashed line. We estimate the number counts from a total area of $\sim 32.67\,\mathrm{arcmin^2}$. We quote the number of galaxies per $\mathrm{arcmin^2}$ at the limiting magnitude at the top of the blue vertical line.

where $t_{\rm exp}$ is the exposure time of the *Euclid* observations. In the EWS, this corresponds to 2280 s for the $I_{\rm E}$ band and 448 s for the $Y_{\rm E}$, $J_{\rm E}$, and $H_{\rm E}$ bands (Euclid Collaboration: Scaramella et al. 2022). The limiting flux, $F_{\rm lim}$, was computed from the limiting magnitude, $m_{\rm lim}$, using the zero point introduced in Sect. 3.4:

$$
F_{\rm lim}[\mathrm{e\,s^{-1}}] = 10^{0.4(\mathrm{ZP_{Euclid}} - m_{\rm lim})}. \tag{13}
$$

The expected limiting magnitudes and S/N in the EWS are reported in Table 1 (Euclid Collaboration: Scaramella et al. 2022). The noise was generated using a Poisson process, where the noise variance is equal to the sum of $F_{X,\rm rebin}$ and $\mathrm{BK_{sky}}$. Panel (e) of Fig. 2 shows the resulting simulated *Euclid* image in the $I_{\rm E}$ band, including the noise.

Fig. 3 presents the results of applying the simulation pipeline, from step (a) to (e), to create mock *Euclid* observations in all the photometric bands for a region with an approximate size of $70'' \times 50''$ encompassing the core of the galaxy cluster MACS J0416. The left-hand panels show the input HST photometric data (excluding the HST F814W filter) while the right-hand panels show the output simulated *Euclid* images in the $I_{\rm E}$, $Y_{\rm E}$, $J_{\rm E}$, and $H_{\rm E}$ bands. Despite the shallower depth of the EWS observations compared to the CLASH and HFF observations, many strong lensing features, including some prominent gravitational arcs, are clearly visible in the *Euclid* images. Notably, the higher spatial resolution of the $I_{\rm E}$ band allowed us to distinguish small details, such as stellar clumps and spiral structures, which appear in some of the multiple images of background lensed galaxies. These features are fundamental in constraining the total mass distribution of galaxy clusters through strong gravitational lensing (e.g. Bergamini et al. 2021; Pignataro et al. 2021), as discussed in subsequent sections. Simulated *Euclid* images similar to those presented in this section were created for all 27 galaxy clusters observed during the CLASH and HFF programmes.

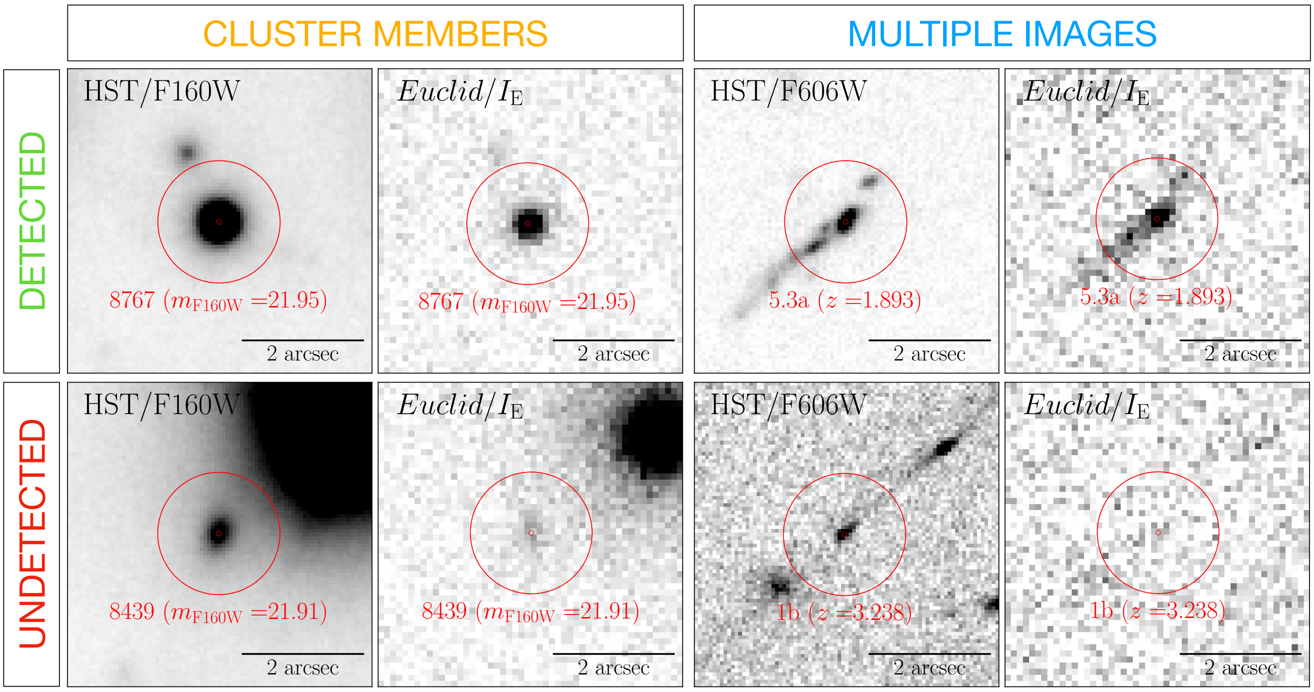

Fig. 6. Comparison between cluster members and multiple images as observed by the HST and *Euclid*. All sources are observed near the core of the galaxy cluster MACS J0416. The upper panels show a cluster member and a lensed galaxy detected in both the HST F160W (HST F606W) and *Euclid* I_E bands. In contrast, the sources in the bottom panels are detected in the HST data but not in the *Euclid* images. In each panel, we report the IDs of the displayed cluster members and multiple images from the catalogues presented by Bergamini et al. (2023), the F160W total magnitude of the cluster galaxies, and the redshift of the lensed sources.

4. Simulation validation

This section discusses three tests performed on the mock *Euclid* images to validate the simulation pipeline. In the first test, we verified that the expected depth of the EWS observations was correctly reproduced in the simulations. In the second, we derived the distribution of the sizes of the galaxies in blank fields. Finally, in the third test, we estimated the number counts of galaxies detected in the *Euclid* images. For tests two and three, we made use of simulated I_E images of six cluster-parallel blank fields obtained during the HFF observations.

The coloured dots in the left panel of Fig. 4 show the measured S/N for the luminous sources identified in the different *Euclid* bands of the galaxy cluster MACS J0416, plotted as a function of their magnitude. These sources include cluster members and galaxies in the cluster foreground or background. Both the S/N and the magnitudes were measured within circular apertures containing 132.7 pixels for the I_E band and 9 pixels for the Y_E, J_E, and H_E filters (see Table 1). The figure shows that for source magnitude values equal to the limiting magnitude, the measured S/N precisely matches the expected EWS value (dashed coloured lines; see also Table 1). This test demonstrates that the noise in the simulated *Euclid* images reproduces the expected depth of the EWS data.

The right panel of Fig. 4 shows the distribution of the circularised FWHM for 1748 galaxies, with I_E magnitudes ≤ 24.5 (i.e. down to the limiting magnitude), identified in the I_E images of the six Euclidised parallel fields described above. The cumulative probability distribution is also plotted in red. This analysis reveals that 93.8% of the selected galaxies have FWHM $\leq 1''.3$, with a median value of $0''.59$. Assuming a Gaussian profile for the galaxy surface brightness distribution and a median FWHM equal to $0''.59$, we find that 96.4% of the brightness of the galaxies is enclosed within an aperture of $0''.65$ radius. This value corresponds to the size of the aperture used to measure the limiting magnitude and S/N in the I_E band (see Table 1).

Finally, Fig. 5 shows the measured distribution of number counts, i.e. the number of detected galaxies per deg^2 per magnitude bin, in the six HFF parallel fields. In the figure, the *Euclid* number counts (grey histogram) are compared with those estimated from HST observations (black curve, Capak et al. 2007). From the cumulative distribution of galaxies (red dashed line), we estimate that the density of resolved galaxies brighter than the limiting magnitude (I_E magnitude ≤ 24.5) is equal to 28 ± 1 galaxies per arcmin^2, in full agreement with expectations for the EWS observations (Laureijs et al. 2011).

5. Parametric strong lensing models of galaxy clusters based on *Euclid* observations

As a possible application of the simulated *Euclid* photometric images, we present a preliminary analysis to quantify the precision and accuracy achievable by parametric strong lensing models of galaxy clusters based on *Euclid* data. Our analysis focuses on the HFF galaxy cluster MACS J0416, for which Bergamini et al. (2023) developed a high-precision strong lensing model (hereafter the B23 model), based on the spectrophotometric data obtained with HST and MUSE. Both the B23 model and the other lens models presented in this work are constructed using the publicly available parametric software `LensTool` (Jullo et al. 2007; Limousin et al. 2005; Jullo & Kneib 2009).

In the B23 model, the total projected gravitational potential of MACS J0416 is expressed as the sum of several contributions,

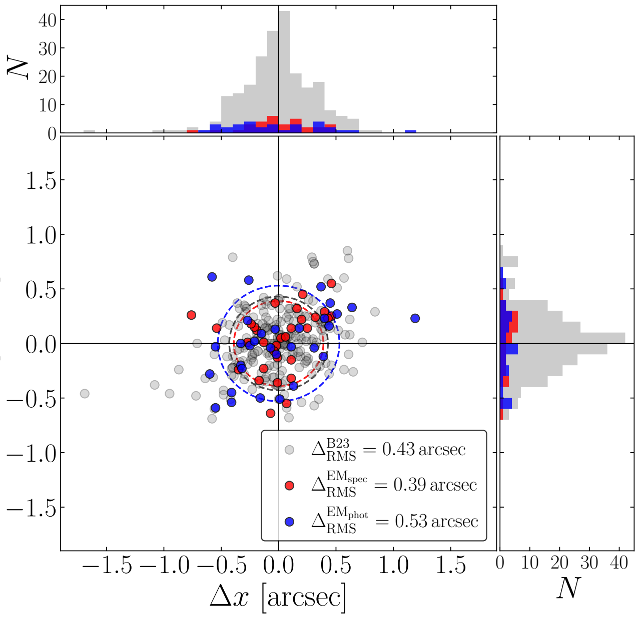

Fig. 7. Displacements in the sky plane between the observed and model-predicted positions of the multiple images. We show the results for the models $\mathrm{EM_{spec}}$ and $\mathrm{EM_{phot}}$ in red and blue, respectively. For comparison, we also show the results obtained by B23 in grey. The histograms show the distribution of the displacements along the two directions. While the B23 model is based on 237 multiple images from 88 background sources, the $\mathrm{EM_{spec}}$ and $\mathrm{EM_{phot}}$ models are constructed using constraints from 31 multiple images of 12 sources. We quantify the accuracy of each model in terms of the $\Delta_{\rm RMS}$ (see Sect. 6), as reported in the legend. This accuracy also determines the radii of the coloured dashed circles in the figure.

each corresponding to a different mass component:

$$\phi_{\rm tot} = \sum_{i=1}^{N_{\rm h}} \phi_i^{\rm halo} + \sum_{j=1}^{N_{\rm G}} \phi_j^{\rm gas} + \sum_{k=1}^{N_{\rm g}} \phi_k^{\rm gal} + \phi^{\rm fg}. \tag{14}$$

The $\phi_i^{\rm halo}$ terms represent the contribution from $N_{\rm h} = 4$ cluster-scale haloes to the total cluster gravitational potential. Three of these haloes are parametrised as elliptical dual pseudo-isothermal mass distributions (dPIEs, Limousin et al. 2005; Elíasdóttir et al. 2007; Bergamini et al. 2019) with an infinite truncation radius: two are centred close to the positions of the two brightest cluster galaxies (BCGs), and one is located in the southern part of the cluster, providing second-order corrections to the total mass distribution in that region. The fourth halo is a circular, non-truncated, dPIE profile that accounts for an overdensity of galaxies in the north-eastern region of the cluster. In addition to these cluster-scale haloes, $N_{\rm G} = 4$ dPIEs ($\phi_j^{\rm gas}$ in Eq. (14)) are used to describe the hot gas content of the cluster. The values of the parameters of these profiles are fixed in the B23 lens model, as they were determined from the analysis of Chandra X-ray data of the cluster performed by Bonamigo et al. (2018). The sub-halo mass component of MACS J0416 (corresponding to the terms $\phi_k^{\rm gal}$ in Eq. (14)) comprises a total of $N_{\rm g} = 213$ cluster member galaxies, including the two BCGs. Of these galaxies, 212 are parametrised as circular, core-less dPIEs, whose central velocity dispersions (σ_0) and truncation radii ($r_{\rm cut}$) are scaled with their luminosities, following the two scaling relations reported in Eq. (4) of Bergamini et al. (2023). The remaining galaxy, identified as Gal-8971, is separately parametrised as an elliptical, core-less dPIE since its total mass is responsible for the formation of a galaxy-galaxy strong lensing system that creates four multiple images of a background source at $z = 3.221$. Finally, the last term in Eq. (14), $\phi^{\rm fg}$, accounts for the contribution to the lensing observables from a single foreground galaxy in the southwestern region of the cluster. This galaxy is described as a circular core-less dPIE.

The optimal values of the free parameters of the profiles defined in Eq. (14) were determined by minimising the following χ^2 function, which quantifies how well the lens model predicts the observed positions of the multiple images:

$$\chi^2(\boldsymbol{\xi}) := \sum_{j=1}^{N_{\rm sou}} \sum_{i=1}^{N_{\rm im}^j} \left(\frac{\left\| \mathbf{x}_{i,j}^{\rm obs} - \mathbf{x}_{i,j}^{\rm pred}(\boldsymbol{\xi}) \right\|}{\Delta x_{i,j}} \right)^2, \tag{15}$$

where $\Delta x_{i,j}$ are the uncertainties on the observed positions of the images, $N_{\rm im}^j$ is the number of multiple images of the same j-th background source, and $N_{\rm sou}$ is the total number of sources. The B23 lens model is constrained by the observed positions of 237 spectroscopically confirmed multiple images from 88 background sources within the redshift range $0.94 \le z \le 6.63$. We refer to Bergamini et al. (2023) for a detailed description of the lens model.

By exploiting the *Euclid* simulated images of the galaxy cluster MACS J0416 in the $I_{\rm E}$, $Y_{\rm E}$, $J_{\rm E}$, and $H_{\rm E}$ bands, we developed two *Euclid*-based lens models, hereafter identified as $\mathrm{EM_{spec}}$ and $\mathrm{EM_{phot}}$. Both $\mathrm{EM_{spec}}$ and $\mathrm{EM_{phot}}$ assume a parametrisation for the total mass of MACS J0416 similar to that adopted in the B23 model, but with the following three important differences. First, the cluster-scale component of MACS J0416 is parametrised by using just two non-truncated dPIE profiles centred on the positions of the BCGs. Second, the hot-gas mass component is not considered (i.e. the $\phi_j^{\rm gas}$ terms are not present in the models). Third, the sub-halo mass component of the cluster contains only those 125 cluster galaxies that are identifiable in the *Euclid* $I_{\rm E}$ band and with an $I_{\rm E}$ magnitude ≤ 22.5 (see Fig. 6). All these galaxies are parametrised as circular, core-less dPIEs, adopting the σ_0–L and $r_{\rm cut}$–L scaling relations mentioned above, where the luminosity L corresponds to the Kron magnitude of the galaxies measured in the $I_{\rm E}$ band (instead of the HST F160W Kron magnitude adopted in the B23 model). Since Gal-8971 now follows the scaling relations, the number of free parameters in the lens model is reduced by four. Thus, the *Euclid*-based lens models count a total of 16 free parameters (12 associated with the parametric profiles used to describe the cluster-scale total mass distribution, two are the normalisations of the σ_0–L and $r_{\rm cut}$–L cluster member scaling relations, and two are used to parameterise the foreground galaxy residing in the south-western region of the cluster). We also note that, contrary to the B23 lens model, we did not assume any Gaussian prior on the normalisation of the σ_0–L scaling relation. In the B23 model, this Gaussian prior is inferred from the measure stellar kinematics of the cluster member galaxies, through the procedure described by Bergamini et al. (2019).

The $\mathrm{EM_{spec}}$ and $\mathrm{EM_{phot}}$ were constrained by the observed positions of 31 multiple images from 12 background sources within the spectroscopic redshift interval $1.01 \le z \le 2.30$. This corresponds to the subsample of multiple images of the original B23 catalogue that were identifiable through visual inspecting the *Euclid* $I_{\rm E}$ simulated observation. The larger pixel scale and lower resolution and depth of the *Euclid* images compared to the original HST data allowed the secure detection of 13% of the multiple images used in the B23 model. Figure 6 shows

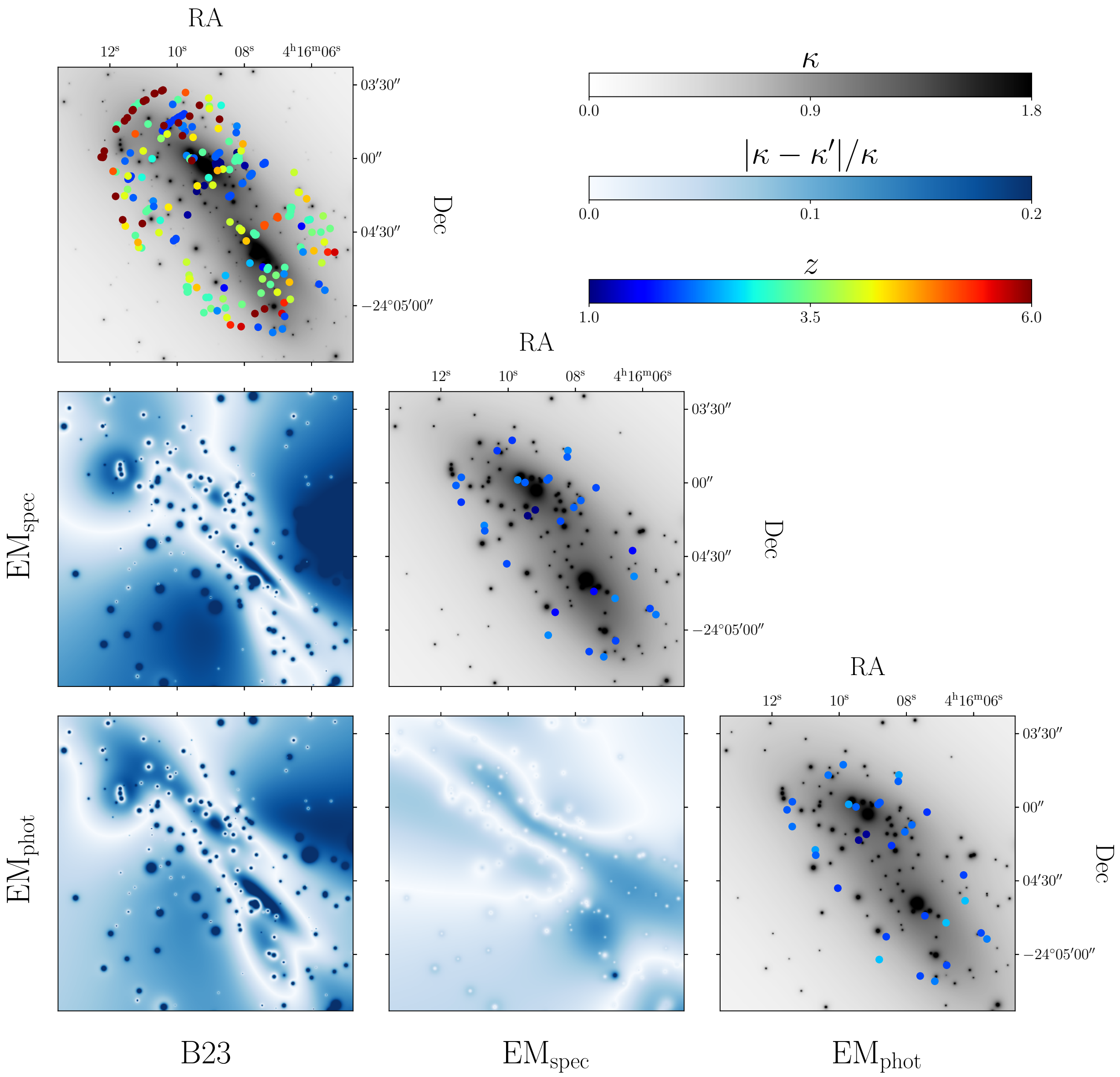

Fig. 8. Comparison between the convergence maps for the galaxy cluster MACS J0416, obtained from the B23, $\mathrm{EM_{spec}}$, and $\mathrm{EM_{phot}}$ strong lensing models. The maps are rescaled such that the ratio of the lens-source and observer-source angular diameter distances equals one. At the top of each column, we show the convergence maps obtained from the different models, while the dots mark the positions of the multiple images. The latter are colour-coded according to their redshifts. The panels at the intersections between pairs of models show the relative difference between the corresponding convergence maps.

examples of detected and non-detected cluster galaxies and multiple images in the I_E image.

The $\mathrm{EM_{spec}}$ and $\mathrm{EM_{phot}}$ models differ in that, while in the former we used the spectroscopic redshifts of the observed multiple images, in the latter we assumed photometric redshift measurements. To simulate the photometric redshift measurements, we randomly extracted, for each source, a redshift value from a Gaussian distribution centred on the source spectroscopic redshift, z_spec, and with a standard deviation equal to $(1 + z_\mathrm{spec})\,0.05$. This corresponds to the expected uncertainty on photometric redshift measurements in the EWS (Laureijs et al. 2011; Euclid Collaboration: Desprez et al. 2020; Euclid Collaboration: Paltani et al. 2024).

We note that $\mathrm{EM_{spec}}$ and $\mathrm{EM_{phot}}$ are optimistic examples of lens models based on *Euclid* data. To construct these models, we used the multiple images and cluster member catalogues from Bergamini et al. (2023), based on HST photometric data and VIMOS and MUSE spectroscopic data, to identify the sources detectable in the *Euclid* simulated observations. In more realistic cases, these components for the strong lensing models will be derived solely from the *Euclid* data. For example, we will identify the cluster galaxies from the observations in the four *Euclid* bands. Angora et al. (2020) show that this task can be accomplished using convolutional neural networks (CNNs). The proposed technique will be tested with simulated *Euclid* images obtained with `HST2EUCLID` in an upcoming paper (Angora et al., in preparation). Spectroscopic follow-up observations will also be critical for identifying pure and complete samples of cluster members and candidate multiple images, as well as for measuring their redshifts. Despite these considerations, our results are informative regarding the precision and accuracy potentially achievable in strong lensing models based on *Euclid* data.

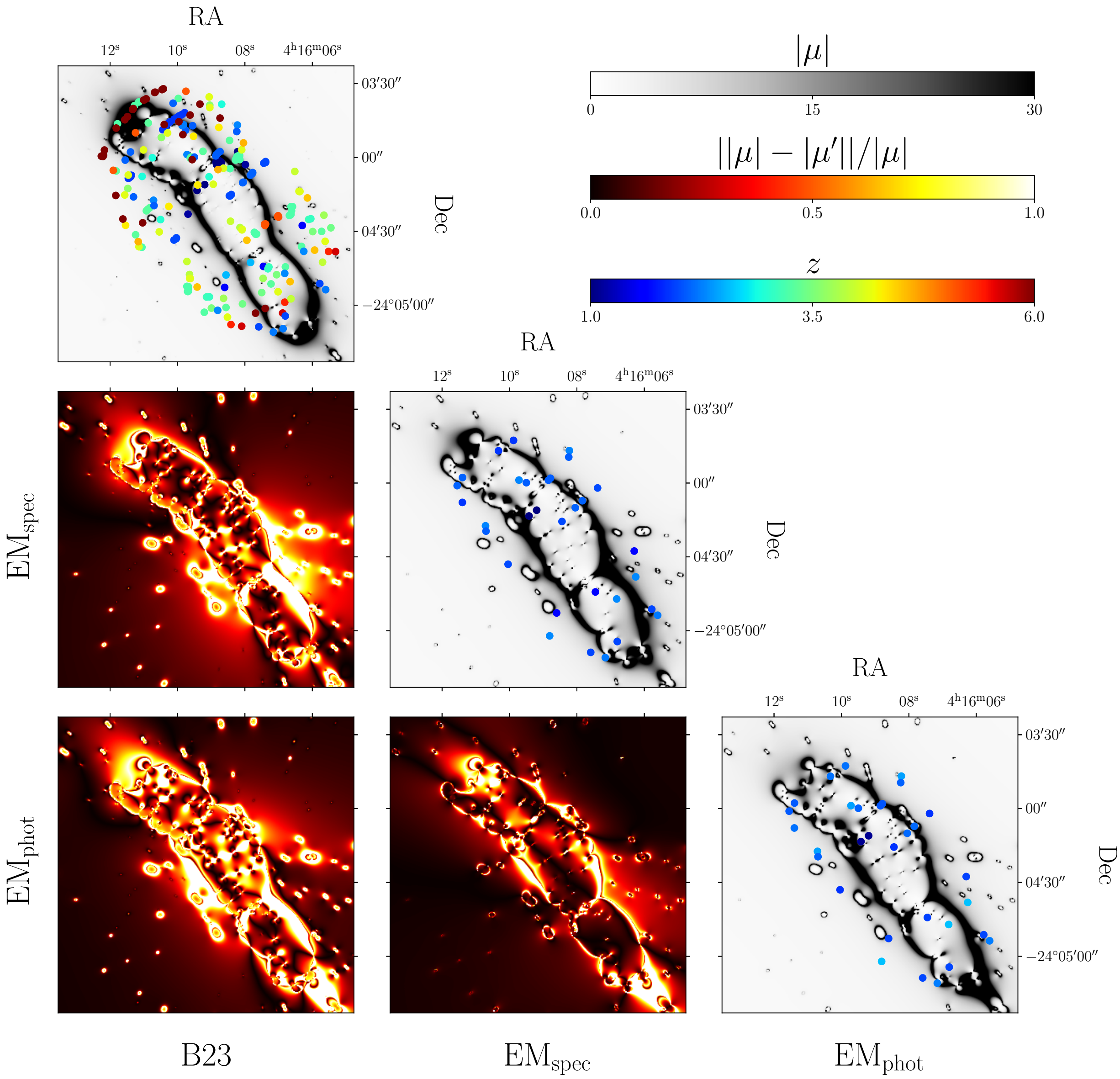

Fig. 9. Comparison between the magnification maps of the galaxy cluster MACS J0416, obtained from the B23, EM$_{\rm spec}$, and EM$_{\rm phot}$ strong lensing models. We show the results for a source at redshift $z = 3$. The model magnification maps are shown at the top of each column. The dots mark the positions of the multiple images, colour-coded according to their redshifts. The panels at the intersections between pairs of models show the relative differences between the corresponding magnification maps.

Previous studies, such as those by Johnson & Sharon (2016) and Meneghetti et al. (2017), discuss how the accuracy and precision of strong lensing models depend on the availability of multiple images and spectroscopic redshifts.

6. Results of the strong lensing analysis on the simulated Euclid clusters

To accurately constrain the total mass distribution of galaxy clusters using strong gravitational lensing, it is crucial to determine the positions of a large sample of multiple images from numerous background sources at different redshifts. Likewise, identifying a pure and complete sample of cluster member galaxies is essential for characterising the sub-halo component of the clusters. Additionally, due to degeneracies between lens model parameters, an inaccurate characterisation of the sub-halo mass distribution can introduce biases in determining the other components in Eq. (14).

Figure 7 shows the displacements in the sky plane between the observed and model-predicted positions for the multiple images of the EM$_{\rm spec}$ (red) and EM$_{\rm phot}$ (blue) models compared to those obtained from the reference lens model by Bergamini et al. 2023 (light grey). We quantified the precision of each model in terms of the root-mean-square separation ($\Delta_{\rm RMS}$) between the observed ($\mathbf{x}^{\rm obs}$) and model-predicted ($\mathbf{x}^{\rm pre}$) positions of the multiple images:

$$\Delta_{\rm RMS} = \sqrt{\frac{1}{N_{\rm im}^{\rm tot}} \sum_{i=1}^{N_{\rm im}^{\rm tot}} \left\| \mathbf{x}_i^{\rm pred} - \mathbf{x}_i^{\rm obs} \right\|^2}, \tag{16}$$

where $N_{\rm im}^{\rm tot}$ is the total number of images in the model.

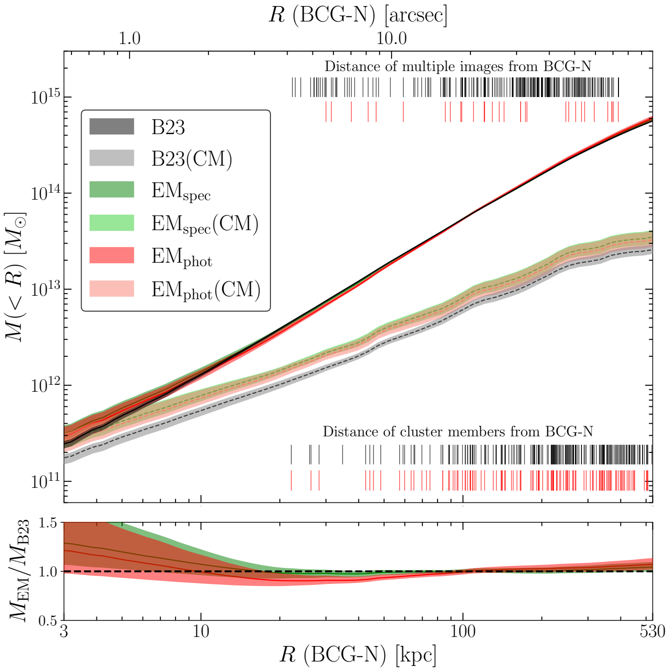

Fig. 10. Top panel: Cumulative total mass profiles of MACS J0416 as derived from the B23, $\mathrm{EM_{spec}}$, and $\mathrm{EM_{phot}}$ strong lensing models. We show the results for the three models using dark grey, green, and red colours, respectively. The coloured bands indicate the 68.3% confidence intervals. We also show the cumulative total mass profiles for the cluster member component (CM) using lighter colours. The radial distances are measured with respect to the BCG-N. We indicate the positions of multiple images and cluster members used in the *Euclid*-based and B23 models with red and black vertical sticks at the top and bottom of the figure, respectively. Bottom panel: Ratios between the cumulative total mass profiles derived from the *Euclid*-based and the B23 models. The coloured bands indicate the 68.3% confidence intervals.

The $\mathrm{EM_{phot}}$ model is characterised by a $\Delta_\mathrm{RMS}^{\mathrm{EM_{phot}}} = 0\farcs53$ in predicting the positions of the multiple images, which is approximately 33% higher than the other two models. This increased Δ_RMS is attributed to weaker lensing constraints from the less accurate photometric redshift measurements, as opposed to spectroscopic redshifts, for the lensed background sources. In contrast, the $\mathrm{EM_{spec}}$ predicts the positions of the observed multiple images with a Δ_RMS of $0\farcs39$, which is about 9% smaller than for the B23 model ($0\farcs43$). This minor discrepancy is due to the differing number of degrees of freedom (DoF, see Eq. (4) in Bergamini et al. 2021) in the two lens models. The $\mathrm{EM_{spec}}$ must reproduce the positions of 31 multiple images from 12 background sources (i.e. about 13% of the images considered in the B23 model), using 16 free parameters (22 DoF), whereas the B23 model predicts 237 multiple images from 88 sources with 30 free parameters (268 DoF). Therefore, the considerably higher number of DoF in the latter lens model makes it less prone to overfitting, albeit at the cost of a larger Δ_RMS (see Fig. 7).

In Figs. 8 and 9, we compare the convergence and magnification maps obtained from the three lens models. The results are shown on a grid of panels (i, j), where the indices $i, j \in [1, 3]$ identify the lens models. Thus, the maps from the i-th lens model are displayed along the diagonal ($i = j$) of the figures. The model names are reported at the bottom of each column and on the left side of each row of panels. The panels in the i–th row and j–th column show the relative differences between the maps of models j and i.

We note that while the convergence maps of the $\mathrm{EM_{spec}}$ and $\mathrm{EM_{phot}}$ models are quite similar, with a median absolute relative difference of ∼4% (second panel in the bottom row), larger discrepancies exist between these models and the B23 model (first column of panels). This is expected, given the different total mass parametrisations adopted in the *Euclid* and HST-based lens models. As described in Sect. 5, the large-scale total mass distribution of MACS J0416 in the $\mathrm{EM_{spec}}$ and $\mathrm{EM_{phot}}$ is parametrised using only two elliptical dPIEs, in contrast to the four included in the B23 model. The two additional haloes in the latter model (a circular one north-east of the northern BCG and a highly elliptical one close to the southern BCG) are clearly identifiable in the panels in the first column of Fig. 8. They correspond to regions of large relative differences between the maps. The models also differ at galaxy scales due to the lower number of cluster galaxies included in the *Euclid*-based lens models (125 out of 213 in the B23 model), and due to the absence of the Gaussian prior on the value of the normalisation of the σ_0–L scaling relation used to model the cluster galaxies (see Sect. 5). In particular, the mass in galaxy-scale haloes in the *Euclid*-based lens models is larger than in the B23 model (see Fig. 10). Some of the differences between the models are also due to the lack of large-scale haloes describing the hot gas mass distribution in the $\mathrm{EM_{spec}}$ and $\mathrm{EM_{phot}}$ models.

The *Euclid*-based models also exhibit similar magnification patterns, as shown in Fig. 9. However, the magnification is derived from the second spatial derivatives of the lensing potential (Meneghetti 2021). Thus, even small differences between the model mass distributions can lead to large variations in magnification on small scales. These variations are most significant along the critical lines, i.e. the lines where the magnification diverges. The differences are larger when the *Euclid*-based maps are compared to the B23 model. For example, the region along the northern section of the cluster critical lines exhibits large variations between the *Euclid*-based and B23 models. The $\mathrm{EM_{spec}}$ and $\mathrm{EM_{phot}}$ models lack constraints in this region. Most of the multiple images detected in the HST data are too faint to be detected by *Euclid*, as they originate from distant sources at $z \gtrsim 6$.

Despite these differences, both the $\mathrm{EM_{spec}}$ and $\mathrm{EM_{phot}}$ models can be used to accurately measure the total projected mass profile in the cluster core. In the upper panel of Fig. 10, we present the cumulative mass profiles derived from the different lens models. We show profiles for both the total mass distributions and the cluster member (CM) components. We report the ratios between the mass profiles derived from the *Euclid*-based and B23 models in the bottom panel. The radius R is measured with respect to the position of the northern BCG (BCG-N). The total cumulative mass profiles agree at the level of $\lesssim$5% in the radial range covered by the strong lensing constraints, as indicated by the vertical segments at the top of the figure. Significant deviations between the *Euclid*-based models and the B23 model arise only at distances smaller than ~ 10 kpc from BCG-N. This result is not surprising, as strong lensing is a robust estimator of the total mass within the Einstein radius (i.e. within the lens critical lines; Meneghetti et al. 2017). However, as highlighted earlier, the *Euclid*-based models measure a larger mass in cluster members compared to the B23 model. Disentangling the large- and small-scale mass components of the cluster requires additional constraints derived from stellar kinematics measurements (e.g. Bergamini et al. 2019, 2021).

Although not shown in Fig. 10, strong lensing alone is unable to constrain the mass profile far outside the region

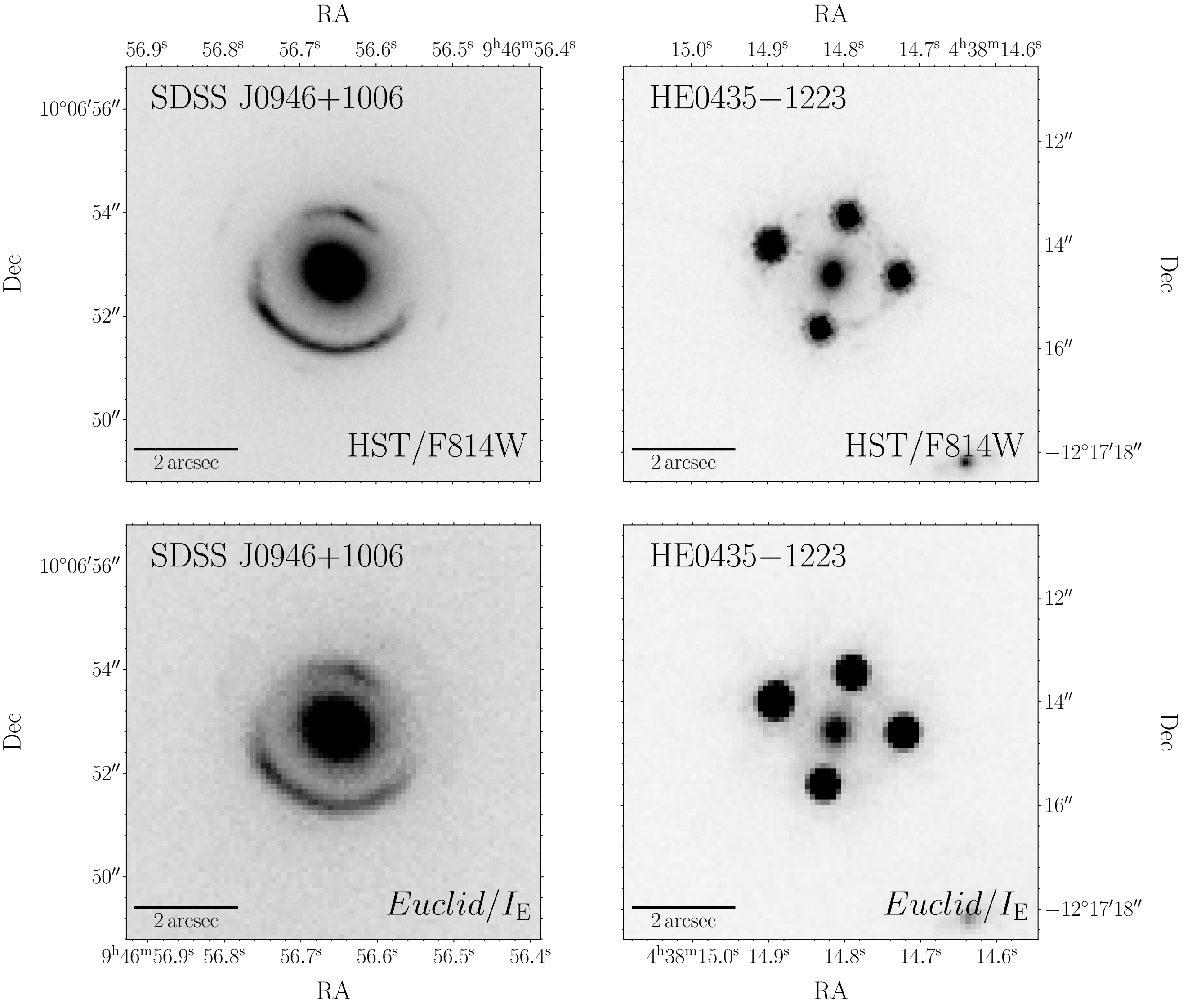

Fig. 11. Examples of simulated *Euclid* images of galaxy-galaxy strong lensing systems as observed during the *Euclid* wide survey. In the upper panels, we show the two HST images used to generate the simulations in the lower panels. The system on the left, identified as SDSS J0946+1006 (also known as the Jackpot lens), consists of a double Einstein ring lensed by a galaxy at $z = 0.222$ (at the centre of the image). The HE0435−1223 system on the right is a quadruple imaged quasi-stellar object (QSO) at $z = 1.693$ lensed by a galaxy at $z = 0.455$.

containing the multiple images. However, due to its large field of view and survey strategy, *Euclid* will measure the shear out to the virial radius and beyond, at least for massive galaxy clusters (Euclid Collaboration: Giocoli et al. 2024; Euclid Collaboration: Lesci et al. 2024). Several studies have demonstrated that combining weak and strong lensing enhances the precision and accuracy of mass profile measurements out to large radii (e.g. Meneghetti et al. 2010). Moreover, mapping the two-dimensional mass distributions within large regions around the cluster centre allows us to characterise complex mass distributions such as merging clusters and filaments (Bradač et al. 2006; Merten et al. 2011, 2015; Diego et al. 2023).

7. `HST2EUCLID` applications

Although this work mainly focuses on the analysis of EWS-like data of galaxy clusters, the `HST2EUCLID` code is designed to simulate customised *Euclid* imaging observations. In particular, one can use any kind of HST image as an input and specify a number of parameters (exposure times, PSF models, limiting magnitude, and S/N) to generate mock images. As an example, Fig. 11 shows simulated *Euclid* images of two galaxy-galaxy strong lensing systems, as observed in the EWS. The system shown in the left panels of the figure is identified as SDSS J0946+1006, also known as the Jackpot lens, and consists of a double Einstein ring lensed by a galaxy at $z = 0.222$ (at the centre of the left images). The inner ring, with a radius of approximately $1\farcs4$, has a redshift of $z = 0.609$, while the outer ring, with a radius of $\sim2\farcs1$, has $z = 2.035$ (Gavazzi et al. 2008). A third source at $z = 5.975$ is also lensed in two additional multiple images (Collett & Smith 2020). The system shown in the right panels is instead a quadruple imaged quasi-stellar object (QSO) at $z = 1.693$, lensed by a galaxy at $z = 0.455$, known as HE0435−1223 (Wisotzki et al. 2002; Bonvin et al. 2017). Fig. 12 shows a simulated preview of a portion of the *Chandra* Deep Field South (Giacconi et al. 2002) that will be observed in the *Euclid* Deep Survey (EDS). This simulation assumes an exposure time of 90 744 s and a limiting S/N of 15.9 for a source with an

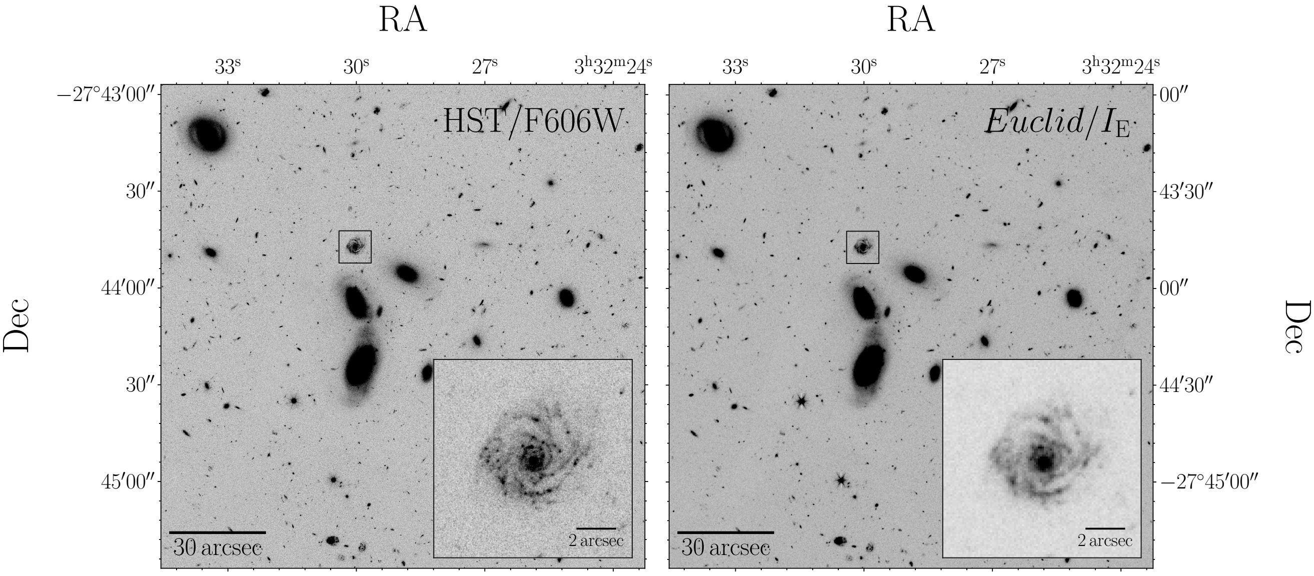

Fig. 12. Comparison between a 150″ × 150″ portion of the *Chandra* Deep Field South as seen by HST (real data) or *Euclid* (simulated). An exposure time of 90 744 s and a limiting magnitude of 26.5, corresponding to the expected depth of the *Euclid* deep fields, is assumed in the simulation.

I_E magnitude of 26.5, measured within a circular aperture of 0″.65 radius. These values correspond to the EDS expected requirements.

Since `HST2EUCLID` is fully modular, it can be easily generalised to simulate a wide range of imaging data. Although this work focuses on converting HST to *Euclid* data, the software can be extended to include multiple input and output instruments, provided that the input images have higher spatial resolution and depth than the simulated output observations. In this context, the new JWST and the future Extremely Large Telescope (ELT) data can be used to generate the simulations. The JWST data can also be used to fully cover the H_E filter as discussed in Sect. 3.3.

Another possible application of the `HST2EUCLID` code, beyond testing the accuracy of *Euclid*-based strong lensing models, is the search for transient sources (e.g. supernovae and active galactic nuclei) in previously observed HST (or JWST) fields. In particular, a direct comparison between the upcoming real *Euclid* data and simulated images allows the identification of transient sources by subtracting the simulated images (before the addition of noise; step d of the simulation pipeline presented in Sect. 3 and Fig. 2) from the real observations of the same region. This application is particularly useful for identifying multiple imaged variable sources lensed by galaxy clusters, such as lensed supernovae. The time delays measured between multiple images of these sources can then be used to constrain cosmological parameter values through the time-delay cosmography technique (e.g. Grillo et al. 2020; Treu et al. 2022; Acebron et al. 2023).

In addition, `HST2EUCLID` can be used to provide the training set for CNN-based techniques aimed at identifying cluster members, galaxy-scale lensing systems, and strong lensing features in clusters (e.g. Angora et al. 2020, 2023; Bazzanini et al., in prep.). More generally, mock HST fields with extensive spectroscopic information are crucial for validating the performance of *Euclid* across a range of legacy science cases (e.g. the search for high-z dropout galaxies and morphological characterisation of galaxies at various redshifts).

8. Conclusions

In this article, we present the `HST2EUCLID` code developed to create simulated *Euclid* images in the I_E, Y_E, J_E, and H_E bands using real HST observations in the ACS F606W, ACS F814W, WFC3 F105W, WFC3 F125W, and WFC3 F160W filters. The code is written entirely in `Python` and can be easily customised for a wide range of studies that make use of *Euclid* images. A high-level interface based on textual input files allows users to access the full functionalities of the code. As a preliminary application, we used `HST2EUCLID` to simulate EWS data for 27 clusters observed by the HST during the CLASH and HFF surveys (21 CLASH and 6 HFF clusters). The cluster redshifts range from 0.19 to 0.89.

By using the simulated *Euclid* images of the galaxy cluster MACS J0416, we tested the possibility of developing high-precision strong lensing models of galaxy clusters based on *Euclid* data. Our results demonstrate that the *Euclid*-based lens models are sufficiently accurate to yield precise estimates of the total mass within the cluster critical lines.

The precision and accuracy achievable with *Euclid*-based lens models rely on the identification of multiple images and cluster members. Both types of sources serve as inputs for constructing the lens models. In this context, redshift measurements from spectroscopic follow-up campaigns will be essential. However, machine and deep learning techniques can automate the search for these sources. Given the paucity of known lenses, especially on the scale of galaxy clusters, training deep learning models requires realistic and sophisticated image simulations, which `HST2EUCLID` can deliver. For instance, strongly lensed galaxies can be injected into Euclidised HST images to construct a training set (Angora et al., in prep.; Bazzanini et al., in prep.).

Despite our work mainly focusing on analysing EWS-like data of galaxy clusters, the `HST2EUCLID` code is designed to simulate any kind of *Euclid* imaging data.

Acknowledgements. We acknowledge financial support through grants PRIN-MIUR 2017WSCC32 and 2020SKSTHZ. PB acknowledges financial support from ASI through the agreement ASI-INAF n. 2018-29-HH.0. MM acknowledges support from the Italian Space Agency (ASI) through contract "Euclid – Phase E" and "Euclid – Phase D". LB is indebted to the communities behind the multiple free, libre, and open-source software packages on which we all depend on. The Euclid Consortium acknowledges the European Space Agency and a number of agencies and institutes that have supported the development of *Euclid*, in particular the Agenzia Spaziale Italiana, the Austrian Forschungsförderungsgesellschaft funded through BMK, the Belgian Science Policy, the Canadian Euclid Consortium, the Deutsches Zentrum für Luft- und Raumfahrt, the DTU Space and the Niels Bohr Institute in Denmark, the French Centre National d'Etudes Spatiales, the Fundação para a Ciência e a Tecnologia, the Hungarian Academy of Sciences, the Ministerio de Ciencia, Innovación y Universidades, the National Aeronautics and Space Administration, the National Astronomical Observatory of Japan, the Netherlandse Onderzoekschool Voor Astronomie, the Norwegian Space Agency, the Research Council of Finland, the Romanian Space Agency, the State Secretariat for Education, Research, and Innovation (SERI) at the Swiss Space Office (SSO), and the United Kingdom Space Agency. A complete and detailed list is available on the *Euclid* web site (`www.euclid-ec.org`). This work uses the following software packages: `Astropy` (Astropy Collaboration 2013, 2018), `matplotlib` (Hunter 2007), `NumPy` (van der Walt et al. 2011; Harris et al. 2020), `Python` (Van Rossum & Drake 2009), `Scipy` (Virtanen et al. 2020), `acstools` (Lim et al. 2020), `reproject`, `argparse`, `re`, `pickle`, `os`, `photutils` (Bradley et al. 2023).

References

Acebron, A., Schuldt, S., Grillo, C., et al. 2023, A&A, 680, L9
Angora, G., Rosati, P., Brescia, M., et al. 2020, A&A, 643, A177
Angora, G., Rosati, P., Meneghetti, M., et al. 2023, A&A, 676, A40
Astropy Collaboration (Robitaille, T. P., et al.) 2013, A&A, 558, A33
Astropy Collaboration (Price-Whelan, A. M., et al.) 2018, AJ, 156, 123
Bacon, R., Accardo, M., Adjali, L., et al. 2012, Messenger, 147, 4
Bartelmann, M., Limousin, M., Meneghetti, M., & Schmidt, R. 2013, Space Sci. Rev., 177, 3
Bayliss, M. B., Hennawi, J. F., Gladders, M. D., et al. 2011, ApJS, 193, 8
Bergamini, P., Rosati, P., Mercurio, A., et al. 2019, A&A, 631, A130
Bergamini, P., Rosati, P., Vanzella, E., et al. 2021, A&A, 645, A140
Bergamini, P., Grillo, C., Rosati, P., et al. 2023, A&A, 674, A79
Boldrin, M., Giocoli, C., Meneghetti, M., & Moscardini, L. 2012, MNRAS, 427, 3134
Boldrin, M., Giocoli, C., Meneghetti, M., et al. 2016, MNRAS, 457, 2738
Bonamigo, M., Grillo, C., Ettori, S., et al. 2018, ApJ, 864, 98
Bonvin, V., Courbin, F., Suyu, S. H., et al. 2017, MNRAS, 465, 4914
Bradač, M., Schneider, P., Lombardi, M., & Erben, T. 2005, A&A, 437, 39
Bradač, M., Clowe, D., Gonzalez, A. H., et al. 2006, ApJ, 652, 937
Bradley, L., Sipőcz, B., Robitaille, T., et al. 2023, `https://doi.org/10.5281/zenodo.7946442`
Capak, P., Aussel, H., Ajiki, M., et al. 2007, ApJS, 172, 99
Coe, D., Fuselier, E., Benítez, N., et al. 2008, ApJ, 681, 814
Collett, T. E., & Smith, R. J. 2020, MNRAS, 497, 1654
Cropper, M., Pottinger, S., Niemi, S., et al. 2016, in Space Telescopes and Instrumentation 2016: Optical, Infrared, and Millimeter Wave, eds. H. A. MacEwen, G. G. Fazio, M. Lystrup, et al., Society of Photo-Optical Instrumentation Engineers (SPIE) Conference Series, 9904, 99040Q
Diego, J. M., Protopapas, P., Sandvik, H. B., & Tegmark, M. 2005, MNRAS, 360, 477
Diego, J. M., Meena, A. K., Adams, N. J., et al. 2023, A&A, 672, A3
Ebeling, H., Edge, A. C., & Henry, J. P. 2001, ApJ, 553, 668
Ebeling, H., Barrett, E., Donovan, D., et al. 2007, ApJ, 661, L33
Ebeling, H., Edge, A. C., Mantz, A., et al. 2010, MNRAS, 407, 83
Elíasdóttir, Á., Limousin, M., Richard, J., et al. 2007, arXiv e-prints [arXiv:`0710.5636`]
Euclid Collaboration (Desprez, G., et al.) 2020, A&A, 644, A31
Euclid Collaboration (Giocoli, C., et al.) 2024, A&A, 681, A67
Euclid Collaboration (Lesci, G. F., et al.) 2024, A&A, 684, A139
Euclid Collaboration (Mellier, Y., et al.) 2025, A&A, 697, A1
Euclid Collaboration (Paltani, S., et al.) 2024, A&A, 681, A66
Euclid Collaboration (Scaramella, R., et al.) 2022, A&A, 662, A112
Euclid Collaboration (Schirmer, M., et al.) 2022, A&A, 662, A92
Gavazzi, R., Treu, T., Koopmans, L. V. E., et al. 2008, ApJ, 677, 1046
Giacconi, R., Zirm, A., Wang, J., et al. 2002, ApJS, 139, 369
Granata, G., Mercurio, A., Grillo, C., et al. 2022, A&A, 659, A24
Grillo, C., Rosati, P., Suyu, S. H., et al. 2020, ApJ, 898, 87
Harris, C. R., Millman, K. J., van der Walt, S. J., et al. 2020, Nature, 585, 357
Hogg, D. W., Baldry, I. K., Blanton, M. R., & Eisenstein, D. J. 2002, arXiv e-prints [arXiv:`astro-ph/0210394`]
Hunter, J. D. 2007, Comput. Sci. Eng., 9, 90
Johnson, T. L., & Sharon, K. 2016, ApJ, 832, 82
Jullo, E., & Kneib, J.-P. 2009, MNRAS, 395, 1319
Jullo, E., Kneib, J.-P., Limousin, M., et al. 2007, New J. Phys., 9, 447
Kneib, J.-P., & Natarajan, P. 2011, A&ARv, 19, 47
Kneib, J., Mellier, Y., Fort, B., & Mathez, G. 1993, A&A, 273, 367
Lam, D., Broadhurst, T., Diego, J. M., et al. 2014, ApJ, 797, 98
Laureijs, R., Amiaux, J., Arduini, S., et al. 2011, arXiv e-prints [arXiv:`1110.3193`]
Liesenborgs, J., De Rijcke, S., & Dejonghe, H. 2006, MNRAS, 367, 1209
Lim, P. L., Davis, M., Hack, W., et al. 2020, Astrophysics Source Code Library [record ascl:`2011.024`]
Limousin, M., Kneib, J.-P., & Natarajan, P. 2005, MNRAS, 356, 309
Lotz, J., Mountain, M., Grogin, N. A., et al. 2014, American Astronomical Society Meeting Abstracts, 223, 254.01
Lotz, J. M., Koekemoer, A., Coe, D., et al. 2017, ApJ, 837, 97
Maciaszek, T., Ealet, A., Gillard, W., et al. 2022, in Space Telescopes and Instrumentation 2022: Optical, Infrared, and Millimeter Wave, eds. L. E. Coyle, S. Matsuura, & M. D. Perrin, Society of Photo-Optical Instrumentation Engineers (SPIE) Conference Series, 12180, 18
Meneghetti, M. 2021, Introduction to Gravitational Lensing: With Python Examples, Lecture Notes in Physics (Springer International Publishing)
Meneghetti, M., Rasia, E., Merten, J., et al. 2010, A&A, 514, A93
Meneghetti, M., Bartelmann, M., Dahle, H., & Limousin, M. 2013, Space Sci. Rev., 177, 31
Meneghetti, M., Natarajan, P., Coe, D., et al. 2017, MNRAS, 472, 3177
Meneghetti, M., Davoli, G., Bergamini, P., et al. 2020, Science, 369, 1347
Meneghetti, M., Ragagnin, A., Borgani, S., et al. 2022, A&A, 668, A188
Meneghetti, M., Cui, W., Rasia, E., et al. 2023, A&A, 678, L2
Merten, J., Coe, D., Dupke, R., et al. 2011, MNRAS, 417, 333
Merten, J., Meneghetti, M., Postman, M., et al. 2015, ApJ, 806, 4
Moresco, M., Amati, L., Amendola, L., et al. 2022, Liv. Rev. Relat., 25, 6
Oguri, M. 2010, PASJ, 62, 1017
Oke, J. B., & Gunn, J. E. 1983, ApJ, 266, 713
Pence, W. D., Chiappetti, L., Page, C. G., Shaw, R. A., & Stobie, E. 2010, A&A, 524, A42
Pignataro, G. V., Bergamini, P., Meneghetti, M., et al. 2021, A&A, 655, A81
Planck Collaboration XXVII. 2016, A&A, 594, A27
Postman, M., Coe, D., Benítez, N., et al. 2012, ApJS, 199, 25
Sartoris, B., Biviano, A., Fedeli, C., et al. 2016, MNRAS, 459, 1764
Treu, T., Suyu, S. H., & Marshall, P. J. 2022, A&ARv, 30, 8
van der Walt, S., Colbert, S. C., & Varoquaux, G. 2011, Comput. Sci. Eng., 13, 22
Van Rossum, G., & Drake, F. L. 2009, Python 3 Reference Manual (Scotts Valley, CA: CreateSpace)
Virtanen, P., Gommers, R., Oliphant, T. E., et al. 2020, Nat. Methods, 17, 261
Wisotzki, L., Schechter, P. L., Bradt, H. V., Heinmüller, J., & Reimers, D. 2002, A&A, 395, 17
Zitrin, A., & Broadhurst, T. 2009, ApJ, 703, L132
Zitrin, A., Meneghetti, M., Umetsu, K., et al. 2013, ApJ, 762, L30

---

[1] Dipartimento di Fisica "Aldo Pontremoli", Università degli Studi di Milano, Via Celoria 16, 20133 Milano, Italy
[2] INAF-Osservatorio di Astrofisica e Scienza dello Spazio di Bologna, Via Piero Gobetti 93/3, 40129 Bologna, Italy
[3] INFN-Sezione di Bologna, Viale Berti Pichat 6/2, 40127 Bologna, Italy
[4] Dipartimento di Fisica e Scienze della Terra, Università degli Studi di Ferrara, Via Giuseppe Saragat 1, 44122 Ferrara, Italy
[5] INAF-Osservatorio Astronomico di Capodimonte, Via Moiariello 16, 80131 Napoli, Italy
[6] INAF-IASF Milano, Via Alfonso Corti 12, 20133 Milano, Italy
[7] Universita di Salerno, Dipartimento di Fisica "E.R. Caianiello", Via Giovanni Paolo II 132, I-84084 Fisciano (SA), Italy
[8] INFN – Gruppo Collegato di Salerno – Sezione di Napoli, Dipartimento di Fisica "E.R. Caianiello", Universita di Salerno, via Giovanni Paolo II, 132 – I-84084 Fisciano (SA), Italy
[9] Dipartimento di Fisica e Astronomia "Augusto Righi" – Alma Mater Studiorum Università di Bologna, via Piero Gobetti 93/2, 40129 Bologna, Italy
[10] Instituto de Física de Cantabria, Edificio Juan Jordá, Avenida de los Castros, 39005 Santander, Spain
[11] Aix-Marseille Université, CNRS, CNES, LAM, Marseille, France
[12] Institut d'Astrophysique de Paris, UMR 7095, CNRS, and Sorbonne Université, 98 bis boulevard Arago, 75014 Paris, France

[13] STAR Institute, Quartier Agora – Allée du six Août, 19c B-4000 Liège, Belgium
[14] Department of Physics, Centre for Extragalactic Astronomy, Durham University, South Road, Durham DH1 3LE, UK
[15] Department of Physics, Institute for Computational Cosmology, Durham University, South Road, Durham DH1 3LE, UK
[16] INAF-Osservatorio Astronomico di Roma, Via Frascati 33, 00078 Monteporzio Catone, Italy
[17] Minnesota Institute for Astrophysics, University of Minnesota, 116 Church St SE, Minneapolis, MN 55455, USA
[18] Université Paris-Saclay, CNRS, Institut d'astrophysique spatiale, 91405 Orsay, France
[19] ESAC/ESA, Camino Bajo del Castillo s/n., Urb. Villafranca del Castillo, 28692 Villanueva de la Cañada, Madrid, Spain
[20] School of Mathematics and Physics, University of Surrey, Guildford, Surrey GU2 7XH, UK
[21] INAF-Osservatorio Astronomico di Brera, Via Brera 28, 20122 Milano, Italy
[22] IFPU, Institute for Fundamental Physics of the Universe, via Beirut 2, 34151 Trieste, Italy
[23] INAF-Osservatorio Astronomico di Trieste, Via G. B. Tiepolo 11, 34143 Trieste, Italy
[24] INFN, Sezione di Trieste, Via Valerio 2, 34127 Trieste TS, Italy
[25] SISSA, International School for Advanced Studies, Via Bonomea 265, 34136 Trieste TS, Italy
[26] Dipartimento di Fisica e Astronomia, Università di Bologna, Via Gobetti 93/2, 40129 Bologna, Italy
[27] Max Planck Institute for Extraterrestrial Physics, Giessenbachstr. 1, 85748 Garching, Germany
[28] Universitäts-Sternwarte München, Fakultät für Physik, Ludwig-Maximilians-Universität München, Scheinerstrasse 1, 81679 München, Germany
[29] INAF-Osservatorio Astrofisico di Torino, Via Osservatorio 20, 10025 Pino Torinese (TO), Italy
[30] Dipartimento di Fisica, Università di Genova, Via Dodecaneso 33, 16146 Genova, Italy
[31] INFN-Sezione di Genova, Via Dodecaneso 33, 16146 Genova, Italy
[32] Department of Physics "E. Pancini", University Federico II, Via Cinthia 6, 80126 Napoli, Italy
[33] INFN section of Naples, Via Cinthia 6, 80126 Napoli, Italy
[34] Instituto de Astrofísica e Ciências do Espaço, Universidade do Porto, CAUP, Rua das Estrelas, PT4150-762 Porto, Portugal
[35] Faculdade de Ciências da Universidade do Porto, Rua do Campo de Alegre, 4150-007 Porto, Portugal
[36] Dipartimento di Fisica, Università degli Studi di Torino, Via P. Giuria 1, 10125 Torino, Italy
[37] INFN-Sezione di Torino, Via P. Giuria 1, 10125 Torino, Italy
[38] Centro de Investigaciones Energéticas, Medioambientales y Tecnológicas (CIEMAT), Avenida Complutense 40, 28040 Madrid, Spain
[39] Port d'Informació Científica, Campus UAB, C. Albareda s/n, 08193 Bellaterra (Barcelona), Spain
[40] Institute for Theoretical Particle Physics and Cosmology (TTK), RWTH Aachen University, 52056 Aachen, Germany
[41] Institute of Space Sciences (ICE, CSIC), Campus UAB, Carrer de Can Magrans s/n, 08193 Barcelona, Spain
[42] Institut d'Estudis Espacials de Catalunya (IEEC), Edifici RDIT, Campus UPC, 08860 Castelldefels, Barcelona, Spain
[43] Dipartimento di Fisica e Astronomia "Augusto Righi" – Alma Mater Studiorum Università di Bologna, Viale Berti Pichat 6/2, 40127 Bologna, Italy
[44] Instituto de Astrofísica de Canarias, Calle Vía Láctea s/n, 38204 San Cristóbal de La Laguna, Tenerife, Spain
[45] Institute for Astronomy, University of Edinburgh, Royal Observatory, Blackford Hill, Edinburgh EH9 3HJ, UK
[46] Jodrell Bank Centre for Astrophysics, Department of Physics and Astronomy, University of Manchester, Oxford Road, Manchester M13 9PL, UK
[47] European Space Agency/ESRIN, Largo Galileo Galilei 1, 00044 Frascati, Roma, Italy
[48] Université Claude Bernard Lyon 1, CNRS/IN2P3, IP2I Lyon, UMR 5822, Villeurbanne F-69100, France
[49] Institute of Physics, Laboratory of Astrophysics, Ecole Polytechnique Fédérale de Lausanne (EPFL), Observatoire de Sauverny, 1290 Versoix, Switzerland
[50] UCB Lyon 1, CNRS/IN2P3, IUF, IP2I Lyon, 4 rue Enrico Fermi, 69622 Villeurbanne, France
[51] Mullard Space Science Laboratory, University College London, Holmbury St Mary, Dorking, Surrey RH5 6NT, UK
[52] Departamento de Física, Faculdade de Ciências, Universidade de Lisboa, Edifício C8, Campo Grande, PT1749-016 Lisboa, Portugal
[53] Instituto de Astrofísica e Ciências do Espaço, Faculdade de Ciências, Universidade de Lisboa, Campo Grande, 1749-016 Lisboa, Portugal
[54] Department of Astronomy, University of Geneva, ch. d'Ecogia 16, 1290 Versoix, Switzerland
[55] INAF-Istituto di Astrofisica e Planetologia Spaziali, via del Fosso del Cavaliere, 100, 00100 Roma, Italy
[56] INFN-Padova, Via Marzolo 8, 35131 Padova, Italy
[57] Université Paris-Saclay, Université Paris Cité, CEA, CNRS, AIM, 91191 Gif-sur-Yvette, France
[58] Istituto Nazionale di Fisica Nucleare, Sezione di Bologna, Via Irnerio 46, 40126 Bologna, Italy
[59] INAF-Osservatorio Astronomico di Padova, Via dell'Osservatorio 5, 35122 Padova, Italy
[60] Institute of Theoretical Astrophysics, University of Oslo, P.O. Box 1029, Blindern, 0315 Oslo, Norway
[61] Jet Propulsion Laboratory, California Institute of Technology, 4800 Oak Grove Drive, Pasadena, CA 91109, USA
[62] Department of Physics, Lancaster University, Lancaster LA1 4YB, UK
[63] Felix Hormuth Engineering, Goethestr. 17, 69181 Leimen, Germany
[64] Technical University of Denmark, Elektrovej 327, 2800 Kgs. Lyngby, Denmark
[65] Cosmic Dawn Center (DAWN), Denmark
[66] Max-Planck-Institut für Astronomie, Königstuhl 17, 69117 Heidelberg, Germany
[67] Department of Physics and Helsinki Institute of Physics, Gustaf Hällströmin katu 2, University of Helsinki, 00014 Helsinki, Finland
[68] Aix-Marseille Université, CNRS/IN2P3, CPPM, Marseille, France
[69] Université de Genève, Département de Physique Théorique and Centre for Astroparticle Physics, 24 quai Ernest-Ansermet, CH-1211 Genève 4, Switzerland
[70] Department of Physics, P.O. Box 64, University of Helsinki, 00014 Helsinki, Finland
[71] Helsinki Institute of Physics, Gustaf Hällströmin katu 2, University of Helsinki, Helsinki, Finland
[72] European Space Agency/ESTEC, Keplerlaan 1, 2201 AZ Noordwijk, The Netherlands
[73] NOVA optical infrared instrumentation group at ASTRON, Oude Hoogeveensedijk 4, 7991PD Dwingeloo, The Netherlands
[74] Centre de Calcul de l'IN2P3/CNRS, 21 avenue Pierre de Coubertin, 69627 Villeurbanne Cedex, France
[75] INFN-Sezione di Milano, Via Celoria 16, 20133 Milano, Italy
[76] Universität Bonn, Argelander-Institut für Astronomie, Auf dem Hügel 71, 53121 Bonn, Germany
[77] INFN-Sezione di Roma, Piazzale Aldo Moro, 2 – c/o Dipartimento di Fisica, Edificio G. Marconi, 00185 Roma, Italy
[78] Université Côte d'Azur, Observatoire de la Côte d'Azur, CNRS, Laboratoire Lagrange, Bd de l'Observatoire, CS 34229, 06304 Nice cedex 4, France
[79] Université Paris Cité, CNRS, Astroparticule et Cosmologie, 75013 Paris, France
[80] Institut d'Astrophysique de Paris, 98bis Boulevard Arago, 75014 Paris, France
[81] Institut de Física d'Altes Energies (IFAE), The Barcelona Institute of Science and Technology, Campus UAB, 08193 Bellaterra (Barcelona), Spain

[82] School of Mathematics, Statistics and Physics, Newcastle University, Herschel Building, Newcastle-upon-Tyne NE1 7RU, UK
[83] Department of Physics and Astronomy, University of Aarhus, Ny Munkegade 120, DK-8000 Aarhus C, Denmark
[84] Space Science Data Center, Italian Space Agency, via del Politecnico snc, 00133 Roma, Italy
[85] Centre National d'Etudes Spatiales – Centre spatial de Toulouse, 18 avenue Edouard Belin, 31401 Toulouse Cedex 9, France
[86] Institute of Space Science, Str. Atomistilor, nr. 409 Măgurele, Ilfov 077125, Romania
[87] Departamento de Astrofísica, Universidad de La Laguna, 38206 La Laguna, Tenerife, Spain
[88] Dipartimento di Fisica e Astronomia "G. Galilei", Università di Padova, Via Marzolo 8, 35131 Padova, Italy
[89] Institut für Theoretische Physik, University of Heidelberg, Philosophenweg 16, 69120 Heidelberg, Germany
[90] Institut de Recherche en Astrophysique et Planétologie (IRAP), Université de Toulouse, CNRS, UPS, CNES, 14 Av. Edouard Belin, 31400 Toulouse, France
[91] Université St Joseph; Faculty of Sciences, Beirut, Lebanon
[92] Departamento de Física, FCFM, Universidad de Chile, Blanco Encalada 2008, Santiago, Chile
[93] Satlantis, University Science Park, Sede Bld 48940, Leioa-Bilbao, Spain
[94] Infrared Processing and Analysis Center, California Institute of Technology, Pasadena, CA 91125, USA
[95] Instituto de Astrofísica e Ciências do Espaço, Faculdade de Ciências, Universidade de Lisboa, Tapada da Ajuda, 1349-018 Lisboa, Portugal
[96] Universidad Politécnica de Cartagena, Departamento de Electrónica y Tecnología de Computadoras, Plaza del Hospital 1, 30202 Cartagena, Spain
[97] INFN-Bologna, Via Irnerio 46, 40126 Bologna, Italy
[98] Kapteyn Astronomical Institute, University of Groningen, PO Box 800, 9700 AV Groningen, The Netherlands
[99] Dipartimento di Fisica, Università degli studi di Genova, and INFN-Sezione di Genova, via Dodecaneso 33, 16146 Genova, Italy
[100] INAF, Istituto di Radioastronomia, Via Piero Gobetti 101, 40129 Bologna, Italy
[101] Astronomical Observatory of the Autonomous Region of the Aosta Valley (OAVdA), Loc. Lignan 39, I-11020 Nus (Aosta Valley), Italy
[102] ICL, Junia, Université Catholique de Lille, LITL, 59000 Lille, France
[103] ICSC – Centro Nazionale di Ricerca in High Performance Computing, Big Data e Quantum Computing, Via Magnanelli 2, Bologna, Italy
[104] Instituto de Física Teórica UAM-CSIC, Campus de Cantoblanco, 28049 Madrid, Spain
[105] CERCA/ISO, Department of Physics, Case Western Reserve University, 10900 Euclid Avenue, Cleveland, OH 44106, USA
[106] Laboratoire Univers et Théorie, Observatoire de Paris, Université PSL, Université Paris Cité, CNRS, 92190 Meudon, France
[107] Istituto Nazionale di Fisica Nucleare, Sezione di Ferrara, Via Giuseppe Saragat 1, 44122 Ferrara, Italy
[108] Université de Strasbourg, CNRS, Observatoire astronomique de Strasbourg, UMR 7550, 67000 Strasbourg, France
[109] Kavli Institute for the Physics and Mathematics of the Universe (WPI), University of Tokyo, Kashiwa, Chiba 277-8583, Japan
[110] Dipartimento di Fisica – Sezione di Astronomia, Università di Trieste, Via Tiepolo 11, 34131 Trieste, Italy
[111] NASA Ames Research Center, Moffett Field, CA 94035, USA
[112] Bay Area Environmental Research Institute, Moffett Field, California 94035, USA
[113] Institute Lorentz, Leiden University, Niels Bohrweg 2, 2333 CA Leiden, The Netherlands
[114] Institute for Astronomy, University of Hawaii, 2680 Woodlawn Drive, Honolulu, HI 96822, USA
[115] Department of Physics & Astronomy, University of California Irvine, Irvine, CA 92697, USA
[116] Department of Astronomy & Physics and Institute for Computational Astrophysics, Saint Mary's University, 923 Robie Street, Halifax, Nova Scotia B3H 3C3, Canada
[117] Departamento Física Aplicada, Universidad Politécnica de Cartagena, Campus Muralla del Mar, 30202 Cartagena, Murcia, Spain
[118] Department of Physics, Oxford University, Keble Road, Oxford OX1 3RH, UK
[119] CEA Saclay, DFR/IRFU, Service d'Astrophysique, Bât. 709, 91191 Gif-sur-Yvette, France
[120] Institute of Cosmology and Gravitation, University of Portsmouth, Portsmouth PO1 3FX, UK
[121] Department of Computer Science, Aalto University, PO Box 15400, Espoo FI-00 076, Finland
[122] Ruhr University Bochum, Faculty of Physics and Astronomy, Astronomical Institute (AIRUB), German Centre for Cosmological Lensing (GCCL), 44780 Bochum, Germany
[123] DARK, Niels Bohr Institute, University of Copenhagen, Jagtvej 155, 2200 Copenhagen, Denmark
[124] Instituto de Astrofísica de Canarias (IAC), Departamento de Astrofísica, Universidad de La Laguna (ULL), 38200 La Laguna, Tenerife, Spain
[125] Université PSL, Observatoire de Paris, Sorbonne Université, CNRS, LERMA, 75014 Paris, France
[126] Université Paris-Cité, 5 Rue Thomas Mann, 75013 Paris, France
[127] Univ. Grenoble Alpes, CNRS, Grenoble INP, LPSC-IN2P3, 53, Avenue des Martyrs, 38000 Grenoble, France
[128] Department of Physics and Astronomy, Vesilinnantie 5, University of Turku, 20014 Turku, Finland
[129] Serco for European Space Agency (ESA), Camino bajo del Castillo s/n, Urbanizacion Villafranca del Castillo, Villanueva de la Cañada, 28692 Madrid, Spain
[130] ARC Centre of Excellence for Dark Matter Particle Physics, Melbourne, Australia
[131] Centre for Astrophysics & Supercomputing, Swinburne University of Technology, Hawthorn, Victoria 3122, Australia
[132] School of Physics and Astronomy, Queen Mary University of London, Mile End Road, London E1 4NS, UK
[133] Department of Physics and Astronomy, University of the Western Cape, Bellville, Cape Town 7535, South Africa
[134] ICTP South American Institute for Fundamental Research, Instituto de Física Teórica, Universidade Estadual Paulista, São Paulo, Brazil
[135] Oskar Klein Centre for Cosmoparticle Physics, Department of Physics, Stockholm University, Stockholm SE-106 91, Sweden
[136] Astrophysics Group, Blackett Laboratory, Imperial College London, London SW7 2AZ, UK
[137] INAF-Osservatorio Astrofisico di Arcetri, Largo E. Fermi 5, 50125 Firenze, Italy
[138] Dipartimento di Fisica, Sapienza Università di Roma, Piazzale Aldo Moro 2, 00185 Roma, Italy
[139] Centro de Astrofísica da Universidade do Porto, Rua das Estrelas, 4150-762 Porto, Portugal
[140] Institute of Astronomy, University of Cambridge, Madingley Road, Cambridge CB3 0HA, UK
[141] Department of Astrophysics, University of Zurich, Winterthurerstrasse 190, 8057 Zurich, Switzerland
[142] Theoretical astrophysics, Department of Physics and Astronomy, Uppsala University, Box 515, 751 20 Uppsala, Sweden
[143] Department of Physics, Royal Holloway, University of London, Surrey TW20 0EX, UK
[144] Department of Physics and Astronomy, University of California, Davis, CA 95616, USA
[145] Department of Astrophysical Sciences, Peyton Hall, Princeton University, Princeton, NJ 08544, USA
[146] Cosmic Dawn Center (DAWN)
[147] Niels Bohr Institute, University of Copenhagen, Jagtvej 128, 2200 Copenhagen, Denmark
[148] Center for Cosmology and Particle Physics, Department of Physics, New York University, New York, NY 10003, USA
[149] Center for Computational Astrophysics, Flatiron Institute, 162 5th Avenue, 10010 New York, NY, USA